

Stellar Imaging Interferometry

by

Armando de Jesús Yance Orcasita

Thesis submitted in partial fulfillment of the requirements for the degree of

MASTER OF SCIENCE

in

Physics

UNIVERSITY OF PUERTO RICO

MAYAGÜEZ CAMPUS

2003

Approved by:

Mark P.J.L. Chang, Ph.D.
President, Graduate Committee

Date

Héctor Jiménez, Ph.D.
Member, Graduate Committee

Date

Carlos U. Pabón, Ph.D.
Member, Graduate Committee

Date

Robert Acar, Ph.D.
Member, Graduate Committee

Date

Haedeh Gooransarab, Ph.D.
Representative of Graduate Studies

Date

Dorial Castellanos, Ph.D.
Chairperson of the Department

Date

Abstract

This thesis work, developed at the laboratories of the Department of Physics of the University of Puerto Rico, reports the first efforts to build a prototype stellar interferometer with applications to stellar astrophysics. The work is focused in the automation of the key subsystems in the interferometer: the Optical Delay Lines (ODLs). The automation of the mechanical controls that allows displacement of ODL, is achieved through the use of inexpensively built stepper motors and driver cards, using slave processors and implementing control through their parallel ports. Our Objective was to obtain precision displacement of the system that controls the ODL. We found that the motors were able to move 400 nm per step in one direction; with a maximum error of 0.5%, but bidirectional motion has a much larger error in our implementation of the system. In testing the prototype while studying the visibility of the fringes, I found that the polarization effects due to the reflections away from normal incidence are an important factor for the optical design of the interferometer.

Resumen

El presente trabajo de tesis, desarrollado en los laboratorios del Departamento de Física de la Universidad de Puerto Rico, reporta los primeros esfuerzos para construir un prototipo de interferómetro estelar con aplicaciones a la astrofísica estelar. El trabajo está enfocado en la automatización de uno de los subsistemas claves en el interferómetro, como lo son las líneas de retraso óptico. La automatización de los controles mecánicos que permitieron el desplazamiento de las líneas de retraso óptico, se logró a través del uso de motores de paso económicos y tarjetas de control, utilizando procesadores como esclavos, e implementando sus puertos paralelos para alcanzar este propósito. Nuestro objetivo era demostrar que es posible obtener precisión en el desplazamiento del sistema que controla las líneas de retraso óptico. Encontramos que los motores de paso elegidos nos permiten desplazarnos 400 nm por paso únicamente en una dirección, con un error máximo de 0.5%, pero la prueba de movimiento bidireccional presentó un error mucho mayor en nuestra implementación del sistema. En las pruebas que se hicieron a nuestro prototipo se estudió la visibilidad de las franjas, y se halló que los efectos debido a la polarización por las reflexiones fuera de la normal, son un factor importante en el diseño del sistema.

Dedication

To **God**, source of every life.

To my kids **CHRISTIAN** and **JESUS**, the reason to be.

To my dear parents **Ana y Armando, Carmen, Julio** and **Luis Jorge**, the proper example to emulate.

To my dear wife **Karina**, for her unconditional support.

To my brothers **Jehosúa** and **Ana del C.**, my big pride.

To my country **Colombia**, in this time on crisis, for whom I want God to bring peace.

To the city of **Barranquilla**, “Curramba la Bella”, where I was born.

To the **Universidad del Atlántico**, where I received my academic foundation.

Dedicatoria

A **Dios**, fuente de toda creación.

A mis pequeños **CHRISTIAN** y **JESUS**, mi razón de ser.

A mis amados padres **Ana** y **Armando**, **Carmen**, **Julio** y **Luis Jorge**, digno ejemplo a seguir.

A mi querida esposa **KARINA**, mi apoyo incondicional.

A mis hermanos **Jehosúa** y **Ana del C.**, mi mayor orgullo.

A mi país **COLOMBIA**, en estos momentos de crisis, para la cual deseo que el Todopoderoso traiga paz y tranquilidad.

A **BARRANQUILLA**, “Curramba la Bella”, la tierra que me vió nacer.

A la **Universidad del Atlántico**, donde recibí mi formación académica.

Acknowledgement

There have been so many people who have influenced the realization of my dreams that it would be impossible to mention them all, however I wish to give thanks especially to the University of Puerto Rico-RUM who, through the Department of Physics, strengthened my academic education; to my advisor Mark Chang for his unconditional support and his lucid instruction both academically and scientifically; to the PRECISE project, principally to Dr. Domingo Rodríguez and Dr. Nestor Rodríguez, for the financial support they provided; to Omayra López, Carmen Santiago and María Schwarz for being there to help me with all the administrative needs.

I would like to thank, as well, my dearest aunt Carmen Yance and my late grandfather Manuel Yance, who made possible, among other things, my time in Mayagüez; to Sra. Carmen Torres for her constant assistance at all times.

To my professors at the Universidad del Atlántico Jorge Rodríguez and Pablo Vilorio who from the beginning believed in me, as with professors Guillermo

Gutierrez, Oswaldo Dede and Humberto Ruiz who gave me their vote of confidence; to my closest friends Raúl Gómez, José Guerra and Santander Nieto, with whom I shared difficulties during my first days in Puerto Rico; to Aziz Mahfoud, inexhaustible companion in science.

To the Barranquilla Planetarium, where my passion for Astronomy was born, which I shared with the distinguished Sra. Alicia Vergara de Chegwin (R.I.P.), Sra. Berenice Larios de Rodríguez, Dr. Álvaro Jiménez and the other members of the grand family of “Amigos de la Astronomía”; and to all those people who in their way have contributed to the success of this work.

Agradecimientos

Son tantas las personas que han influido en la cristalización de mis sueños que sería imposible mencionarlas a todas, pero quiero dar especialmente las gracias a la Universidad de Puerto Rico-RUM, que por mediación del Departamento de Física, fortaleció mis fundamentos académicos; a mi consejero Mark P.J.L. Chang, por su apoyo incondicional y su instrucción lúcida, tanto en lo académico como en lo científico durante este proceso; al proyecto PRECISE, principalmente al Dr. Domingo Rodríguez y al Dr. Nestor Rodríguez, por el apoyo económico ofrecido; a Omayra López, Carmen Santiago y María Schwarz, por su disposición y actitud positiva frente a mis necesidades administrativas.

También quisiera agradecer a mi queridísima tía Carmen Yance y a mi recordado abuelo Manuel Yance (Q.E.P.D.), quienes hicieron posible, entre otras cosas, mi llegada a Mayagüez; a la Sra. Carmen Torres, por su perenne y constante ayuda.

A mis profesores de la Universidad del Atlántico Jorge Rodríguez y Pablo Vilorio, quienes desde el principio creyeron en mí; igualmente, a los profesores Guillermo

Gutierrez, Oswaldo Dede y Humberto Ruiz quienes me dieron su voto de confianza; a mis amigos más cercanos Raúl Gómez, José Guerra y Santander Nieto, con quienes compartí dificultades durante los primeros días en Puerto Rico; a Aziz Mahfoud, compañero incansable de labor científica.

Al Planetario de Barranquilla, donde se inició mi pasión por la Astronomía, la que compartí con la distinguida señora Alicia Vergara de Chegwin (Q.E.P.D.), M.Sc. Berenice Larios de R., Dr. Álvaro Jiménez y demás miembros de la gran familia “Amigos de la Astronomía”; y a todas aquellas personas quienes a su manera han encauzado este logro.

Contents

List of Tables	xii
List of Figures	xiii
1 Introduction	1
1.1 Previous Concepts in High Resolution Imaging	1
1.2 The Current Work	8
2 Historical Meanderings	13
3 Experimental Setup	21
3.1 Principles of Optical Stellar Interferometry	21
3.2 Electro-Mechanical Devices	27
3.2.1 Creating the Ethernet and Computer Controllers	27
3.2.2 Interferometer ODL Subsystems	28
3.3 Basic Interferometer	40
3.3.1 Qualitative Simulations of an Interferometer	41
3.3.2 Michelson-Morley Interferometer Setup Study	47
3.3.3 Two Direct Beam Interferometer at Focal Plane	52
3.3.4 Michelson Stellar Interferometer	53

4	Results and Discussion	57
4.1	New Analysis for the Fringes	67
4.1.1	Method A	68
4.1.2	Method B	69
5	Conclusion	76
	Appendices	80
A	Matlab Scripts	80
B	Code in C language	83
C	Calculation for the Driver Card Circuit Values	86
C.1	Case 1	86
C.2	Case 2	87
D	Images and Graphs of Data	89

List of Tables

2.1	Events in Early Stellar Interferometry	19
2.2	Milestones in Long Baseline Stellar Interferometry	20

List of Figures

1.1	Comparing a single element telescope (a), and an N element telescope (b) (this case N=10).	3
1.2	(a) Drawing of a telescope in which the intermediate elements have been extracted leaving only one at each end, (b) Sketch of a single telescope with a two hole mask, (c) Intensity profile of the fringes for a circular aperture vs. transverse distance.	5
1.3	Two telescope interferometer with image-plane interferometry configuration.	10
1.4	Schematic of an interferometer.	11
1.5	The Palomar Testbed Interferometer (PTI) delay line carriage	11
2.1	(left) Schematic diagram of 20-foot beam on top of the Hooker Telescope, (right) The 100-inch Hooker Telescope used by Michelson and Pease on Mt. Wilson in California.	15
2.2	The arrangement of the Intensity Interferometer at Narrabri Observatory	17
2.3	Timeline of Stellar Interferometry from 1868 to 1940	19
2.4	Stellar Interferometry from 1950 to 2000	20

3.1	Schematic of a two-element stellar interferometer. S and B are vector quantities, and the source is infinitely far from the instrument.	22
3.2	Schematic setup for the planned laboratory interferometer.	26
3.3	A detailed sketch of the ODLs planned in the Laboratory.	28
3.4	(left) A unipolar stepper motor from an old 5.25" floppy drives, (right) Schematic of the unipolar stepper motor coil layout.	30
3.5	Stepping sequence. The simplest implementation, where only one pole is energised at a time follows steps 1,3,5,7. The more complex stepping sequence shown with all the illustrations gives twice as many stationary positions between steps as the simple sequence.	32
3.6	The rotor of an unipolar stepper motor.	33
3.7	A stator of a unipolar stepper motor	33
3.8	An explanatory sketch of the operation process of a unipolar stepper motor	34
3.9	(a) A unipolar motor controller made from npn bipolar junction transistors (BJTs), (b) Detailed sketch from the unipolar motor controller, and (c) Drawing of the control card.	35
3.10	25-way Female D-Type Connector.	38
3.11	Unipolar stepper motor calibration mount.	39
3.12	Schematic circuit to test the parallel port independence.	40
3.13	Plane wave incident on a finite aperture.	41

3.14	(left) Electric field function of the radial amplitude distribution in the diffraction pattern of a circular aperture, (right) Electric field diffraction of a circular hole simulated with the Matlab script. Note that it is the square of this function that is detected and not this function directly.	43
3.15	(1) Mask with two holes (apertures); (2) interference pattern simulated where we can see the fringes; (3) profile of the interference pattern.	44
3.16	Sequence showing the movement of the fringes (showed as cross sections) when a phase factor is applied in one of the apertures. The displacement is toward right side.	45
3.17	Michelson-Morley Interferometer setup	47
3.18	Spatial filter sketch	49
3.19	(top left) The HeNe laser used in the Michelson-Morley Interferometer; (top right) spatial filter; (below left) beamsplitter used; (below right) the fringes obtained are quite visible.	50
3.20	Visibility versus the optical path difference between the arms.	51
3.21	Schematic of Two Beam Interferometer.	54
3.22	Schematic Michelson Stellar Interferometer.	55
3.23	Schematic Michelson Stellar Interferometer with a ODL.	56
4.1	Detail from the ODLs planned in the Laboratory.	57
4.2	Graph of the calibration data for the stepper motor #1 in one direction @ 1ms of delay between steps.	59

4.3	Calibration graph for the stepper motor #1 in two direction @ 1ms of delay between steps.	60
4.4	(left) First fringes obtained from Direct Two beam Interferometer without polarizer, (right) the same setup but using a vertically aligned polarizer filter.	62
4.5	Fringes obtained from Michelson Stellar Interferometer with ODL. (a) Original image, (b) Image rotated.	62
4.6	Representation in 3-D of the image from Two Direct Beam Interferometer without a polarizer filter.	63
4.7	Profile of the fringes from the Direct Beam Interferometer without polarizer filter.	63
4.8	Visibility vs horizontal profile for the Two Beam Interferometer, (1)without polarizer filter, (2)with polarizer filter horizontally aligned, (3)with polarizer filter vertically aligned. The horizontal lines dashed indicate the corresponding maximum, mean and minimum values of visibility.	65
4.9	Visibility vs horizontal profile for Michelson Stellar Interferometer, (1)without polarizer filter, (2)with polarizer filter horizontally aligned, (3)with polarizer filter vertically aligned. The horizontal lines dashed indicate the corresponding maximum, mean and minimum values of visibility.	66

4.10	Visibility vs horizontal profile for Michelson Compensator. Without polarizer filter. The horizontal lines dashed indicate the corresponding maximum, mean and minimum values of visibility.	67
4.11	Profile of the fringes from the Direct Beam Interferometer without polarizer filter.	68
4.12	Average visibility for the images from the Two Beam Interferometer and the Michelson Stellar Interferometer with and without polarizer filters.	69
4.13	Schematic of the analysis method B.	70
4.14	Fringes after having extracted the pedestal signal.	71
4.15	Average heights for the images from the Two Beam Interferometer and the Michelson Stellar Interferometer with and without polarizer filters.	71
4.16	Setup for the measurements of the phase shift of the reflections.	74
4.17	Relative phase shift between two orthogonal polarization states due reflections.	75
5.1	(left) The proposed design for the ODL and (right) the current design.	79
C.1	Figure shown the circuit with all resistances connected to ground.	86
C.2	Figure showing the current flowing through of a circuit branch.	87
C.3	Sketch used to calculate R_b	88

D.1 Calibration data of the stepper motors #1 @ 10ms of delay in one direction.	89
D.2 Calibration data of the stepper motors #1 @ 1ms of delay in one direction.	90
D.3 Calibration data of the stepper motors #1 @ 0.1ms of delay in one direction.	90
D.4 Calibration data of the stepper motors #2 @ 1ms of delay in one direction.	91
D.5 Calibration data of the stepper motors #3 @ 1ms of delay in one direction.	91
D.6 Calibration data of the stepper motor #1 @ 1 ms in two directions. .	92
D.7 Calibration data of the stepper motor #2 @ 1 ms in two directions. .	92
D.8 Calibration data of the stepper motor #3 @ 1 ms in two directions. .	93
D.9 First fringes obtained from Direct Two beam Interferometer without polarizer.	93
D.10 Fringes from Direct Two beam Interferometer with horizontal polarization filter.	94
D.11 Fringes from Direct Two beam Interferometer with vertical polarization filter.	94
D.12 Graphs of intensity vs pixels for each profile from Direct Two Beam Interferometer without polarizer for 10 horizontal lines selected for the single image.	95

D.13	Graphs of intensity vs pixels for each profile from Direct Two Beam Interferometer with horizontal polarization for 10 horizontal lines selected for the single image.	96
D.14	Graphs of intensity vs pixels for each profile from Direct Two Beam Interferometer with vertical polarization for 10 horizontal lines selected for the single image.	97
D.15	Fringes obtained from Michelson Stellar Interferometer without polarization filter.	98
D.16	Fringes obtained from Michelson Stellar Interferometer with horizontal polarizer.	98
D.17	Fringes obtained from Michelson Stellar Interferometer with vertical polarizer filter.	99
D.18	Graphs of intensity vs pixels for each profile from Michelson Stellar Interferometer without polarization filter for 10 horizontal lines selected for the single image.	100
D.19	Graphs of intensity vs pixels for each profile from Michelson Stellar Interferometer with horizontal polarization filter for 10 horizontal lines selected for the single image.	101
D.20	Graphs of intensity vs pixels for each profile from Michelson Stellar Interferometer with vertical polarization filter for 10 horizontal lines selected for the single image.	102

D.21 Fringes obtained from Michelson Stellar Interferometer with ODL. (a)	
Original image, (b) Image rotated.	103
D.22 Graphs of intensity vs pixels for each profile from Michelson Stellar	
Interferometer with ODL for 10 horizontal lines selected for the single	
image.	104

Chapter 1

Introduction

1.1 Previous Concepts in High Resolution Imaging

Before the invention of the telescope, apart from the Sun and the Moon, the other celestial objects observed by the naked eye appeared as simple points of light in the night. The first observers noted five, among these "stars", which wandered erratically through the night sky. The ancient Greeks called these objects "planets" [$\pi\lambda\alpha\nu\acute{\eta}\tau\eta\zeta$ = "planetis" meaning planet, from the root $\pi\lambda\acute{\alpha}\nu\eta\zeta$ = "planis" meaning wanderer]. These "planets" moved in relation to the background objects. With the invention of the telescope, observers were able to study a totally new aspect of the local universe. The planets that seemed to be simple points of light of the sky, albeit steadier than the flickering stars, revealed their hidden faces: Venus's phases, Saturn's rings and Jupiter's moons amongst other details were seen. With the passing of time advances in astronomical optics led to the redrafting of human knowledge. A "zoo" of astronomical objects of great interest were observed, motivating the desire to study

them in detail. One requirement to carry out these studies is high resolution imaging.

The scientific interest in building instruments to obtain high resolution visible images of astronomical objects is growing. But, how do we increase the effective resolving power of our telescopes? Let us consider the ideal case, in the absence of the atmosphere and with perfect optics, a single telescope of diameter D (see Figure 1.1(a)), where the focussing element is a lens. Note that any equivalent optical system will do, although this will affect the following argument in terms of a numerical proportionality constant. The physical effect that limits the resolution of these telescopes is *diffraction*. The diffraction limit of the circular aperture of the instrument is given by $\theta = 1.22 \frac{\lambda}{D}$, where λ is the wavelength of the light and θ is the minimum angular separation¹ that can be seen with this circular aperture. In other words, the diffraction limit is inversely proportional to the diameter of the aperture and directly proportional to the wavelength observed. We can conclude that the key to increasing θ is the construction of larger telescope diameters. However, when the light of a celestial source comes through the atmosphere, the amplitude and phase of the light waves are perturbed by turbulence in the Earth's atmosphere. Moreover, the atmospheric perturbations vary in time. This represents a barrier making it impossible to reach the theoretical diffraction limit. There is also the practical impossibility of building a monolithic telescope of hundreds of meters of diameter, with the current

¹For example the minimum angular separation so that a stellar binary system can be seen as two separate stars as defined by the Rayleigh criterion.

state-of-the-art technology. These difficulties stimulate the search for other methods to enhance the effective resolution of modern telescopes.

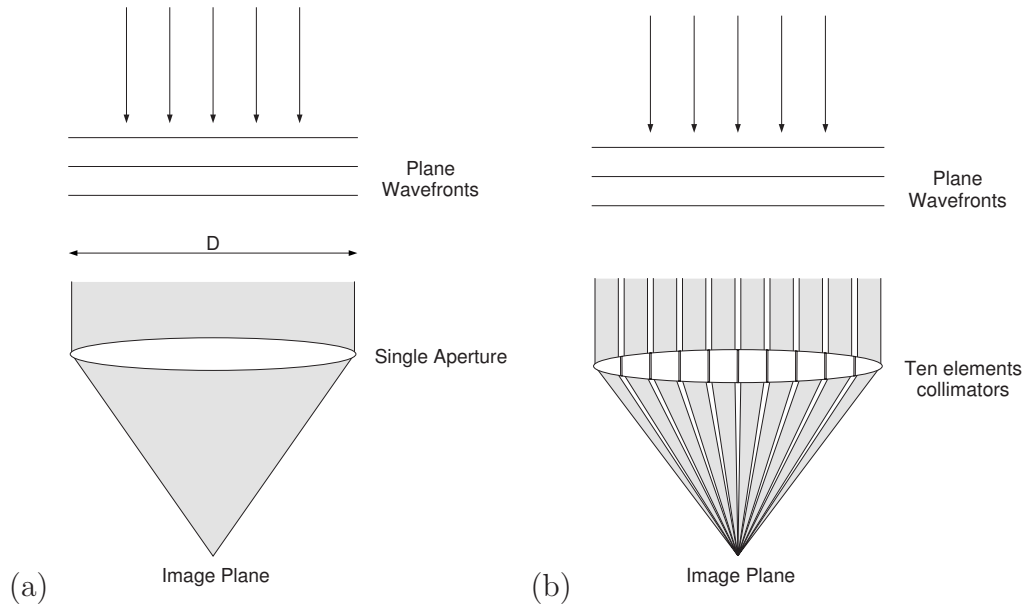


Figure 1.1: Comparing a single element telescope (a), and an N element telescope (b) (this case $N=10$).

So what is a possible solution? For the ideal case outlined previously, let us imagine that we divide the telescope in N equal parts. Due to the geometry of each elemental part, the group collectively functions as a single monolithic telescope, as seen in Figure 1.1(b). The removal of the middle elements leave two single elements, one at each end (See Figure 1.2(a)). Making use of the imaging theory of Abbé, where interference is used to describe image formation, the single element telescope works in the same way as the reduced system of two optical components. In fact a single telescope is an ideal interferometer; the only difference is that, in the two

optical elements, the capacity to capture light rays has diminished. Even at low light levels, the two elements will form an “image” (Figure 1.2(a)). On the other hand, if we cover the aperture of the single telescope with a two hole mask, as in the Figure 1.2(b), we will obtain a system that works as the reduced system previously explained (Figure 1.2(a)). In summary, it is possible to substitute the single telescope aperture with an arrangement of two smaller telescopes apertures separated by a distance equivalent to the diameter of the single telescope. The new composite telescope (now it is convenient to say an interferometer, because it works based on the description provided by the interference of light waves) will have an angular resolution equal to the monolithic lens. The overlapping wavefronts at focus from each small aperture form an interference pattern (Figure 1.2(c)). So, it is very practical to build an “interferometer” instead of a single element telescope, since the construction of an interferometer which has of order a hundred meters of baseline² is feasible, whereas a single telescope of the same diameter is not possible. The motivation for doing so is that the interferometer will provide the same high angular resolution as the (impossibly) large single telescope. The disadvantage, as already said before, is that their capacity of gathering light is reduced. Therefore, this fact sets down a limit to the type of celestial object that we can study by means of an interferometer. That is to say we can not study objects of too low brightness.

For any ground based telescope, the atmosphere induces perturbations in

²Baseline is the distance of separation between the elements in an interferometer.

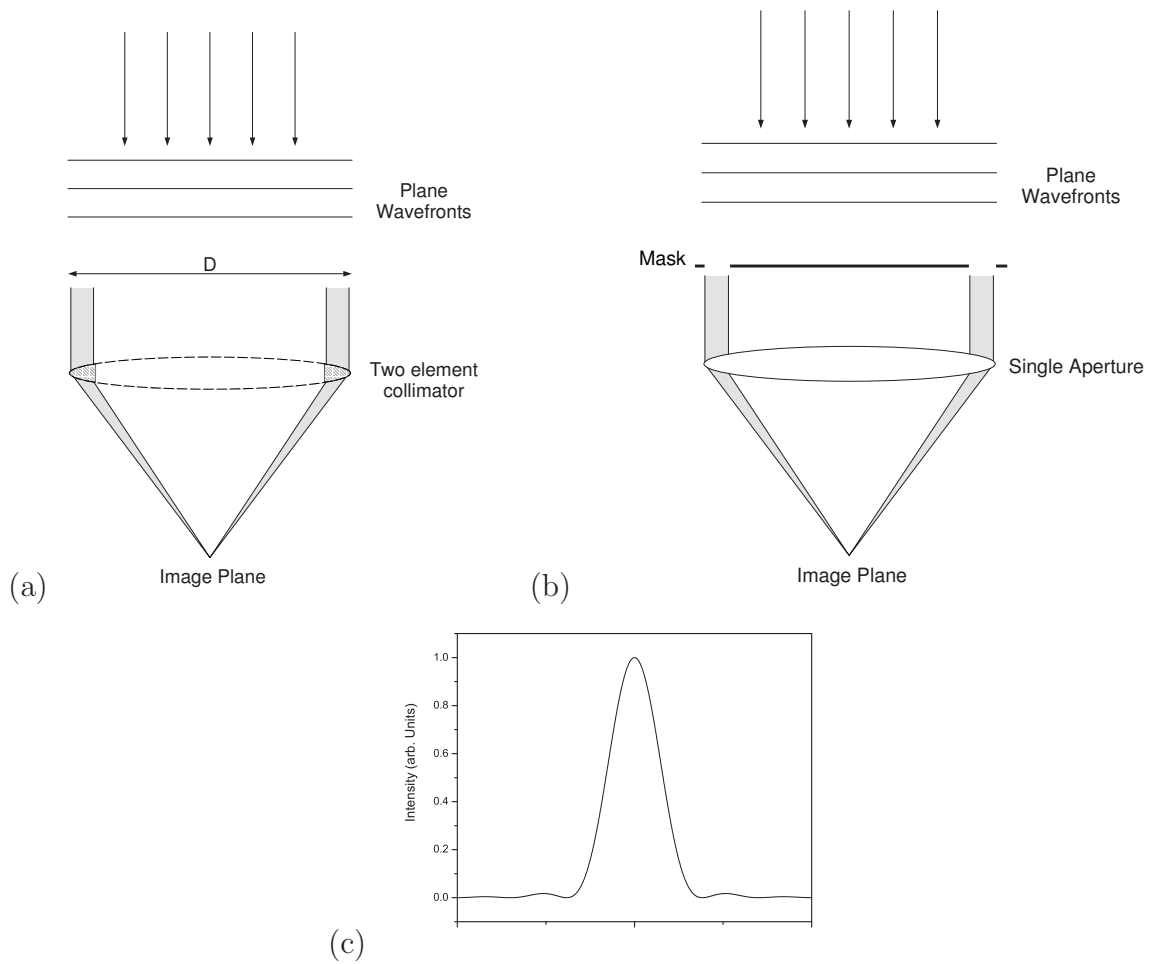


Figure 1.2: (a) Drawing of a telescope in which the intermediate elements have been extracted leaving only one at each end, (b) Sketch of a single telescope with a two hole mask, (c) Intensity profile of the fringes for a circular aperture vs. transverse distance.

the wavefronts of the light that arrives at us, deforming and distorting the images obtained. With our interferometer the situation will be the same, even though in doing interferometry the atmospheric effects can be reduced by having two small apertures, so we may spatially filter the wavefronts received. How can we overcome turbulence? The literature on reducing these effects for single large telescopes indicate that there are two ways of overcoming the Earth's atmospheric induced distortions. One of them is spatially filtering the incident wavefronts. As an example of this there is Speckle Interferometry[1], which consists of reconstructing a star's image starting from many exposures of short³ duration. In each exposure the star's blurred specular image has been frozen. By analyzing the interference fringes in the speckles, the unaberrated image can be reconstructed. Therefore the "filtering" occurs in selecting a single speckle. The other alternative is based on correcting the fluctuations in the wavefronts due to the atmosphere. As an example we have the use of Adaptive Optics (AO), a technique in which the effects of the Earth's atmosphere on the plane wavefronts, coming from the distant source, are sensed and corrected with a deformable mirror plus a wavefront sensing camera before the image is recorded. These improvements are additional to the construction of our interferometer, and we will not go into the details about them, except to state that they are not immediately necessary, provided the apertures of an interferometer are smaller than about one turbulence "cell" size, which is typically 40 cm at 2.2 μm and 12 cm at 0.6 μm for good observing conditions[2].

³Short means shorter than the timescale of the atmospheric changes themselves.

The interest in achieving the high resolution potential in the optical interferometry has motivated the following prototype optical interferometers.

COAST: The Cambridge Optical Aperture Synthesis Telescope (COAST) was planned as an array of four telescopes (40 cm in diameters each), operating in the 0.4-0.95 μm and 2.2 μm with a baseline of 100 m. It is located in Cambridge, UK.

NPOI: The six telescopes of 12.5 cm of diameter, of the Navy Prototype Optical Interferometer (NPOI) at the Lowell Observatory, became the first optical interferometer to track and record stellar interference fringes. This interferometer can work at 0.45-0.9 μm of wavelength and has 437 m of baseline. It is placed in the Anderson Mesa, US and is administered by USNO/NRL.

MRO: The Magdalena Ridge Observatory (MRO), is a joint endeavor between University of Puerto Rico (UPR), New Mexico State University (NMSU), New Mexico Tech, Los Alamos National Laboratory (LANL), and the New Mexico Highlands University (NMHU). The project consists in the design and construction of an optical/IR interferometer of 8 to 10 telescopes of 1.4 m in diameters each. The longest baseline in the array is to be 400 m, working at 0.65-2.4 μm of wavelength(visible/nearinfrared). It is planned that it will be located in New Mexico.

IOTA: The Infrared Optical Telescope Array (IOTA) operates with three 45 cm apertures, at 0.45-0.8 μm and 2.2 μm of wavelength, and reaches a maximum baseline of 38 m. It is placed in Mt. Hopkins, US under the Center for Astrophysics (CfA) administration.

CHARA: The project of Georgia State University's Center for High Angular Resolution Astronomy (CHARA) is an optical/infrared interferometric array of seven-1 m telescopes, located in Mount Wilson, California. This array has a wavelength range of 0.55-0.9 μm and 2.1-2.5 μm , and a maximum baseline of 354 m.

SUSI: The Sydney University Stellar Interferometer (SUSI) at Narrabri, AU. SUSI currently has a maximum baseline of 80 m, and at a prime operating wavelength of 0.42 μm . This interferometer has two collector elements of 14 cm in diameter.

As may be seen, only CHARA and MRO have apertures in the meter range, that is to say, much larger than the coherence size of the atmospheric turbulence effects at the observing wavelengths.

1.2 The Current Work

A two-element interferometer geometry is shown in Figure 1.3, where T_1 and T_2 are the two telescopes to gather the light, M are the mirrors in the system, θ is the angle between the distant source and zenith, D is the baseline, ODL_1 and

ODL₂ are the Optical Delay Lines, L is the image-plane combination system (which is represented by a lens). This interferometer will produce interference fringes (the signal) if the system is correctly aligned, such that the optical path lengths⁴ of its arms are equalised. The optical path is the total distance traveled by the light from the source, through each arm, until it arrives at the combining system where they interfere. In addition to this, the polarisation vectors of the light beams coming from each telescope must be the same. Each reflection from a mirror surface produces a phase shift between the polarization states that is angle dependent. This can cause losses in the contrast of the fringes due to the phase shift. The fringe visibility losses are proportional to the cosines of the phase shift[3].

An interferometer is composed of many subsystems, which are required to align and manoeuvre the system components prior to while observing “on-sky”. Many of them have to be controlled in real-time, and most should be adjustable from a remote station so as not to introduce extra disturbances to the interferometric system.

These requirements imply that one needs quick computerized control. Briefly, the key components within the instrument that need to be computer controlled are (See Figure 1.4):

⁴The optical path is defined to be the refractive index of the medium (usually air) multiplied by the physical path length traversed by the light beam through an optical instrument.

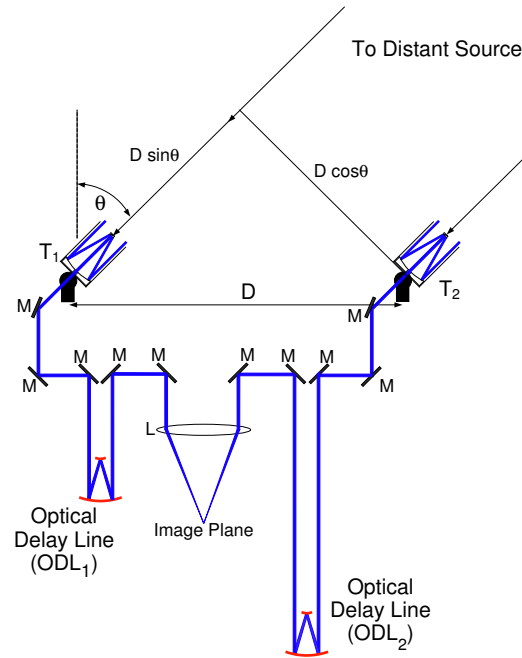


Figure 1.3: Two telescope interferometer with image-plane interferometry configuration.

- A set of artificial sources to align the interferometer components (Alignment system).
- *Optical delay lines*(ODLs) to equalise the arms; one is needed per arm of the instrument.
- Detector positioning system(s) to ensure the fringes are brought into focus on the detection camera (On the combining system).

The ODLs (Figure 1.5) are the key component of an interferometer and generally are extremely expensive to produce. **So the objective of the present work concentrates on the development and implementation of the ODLs**

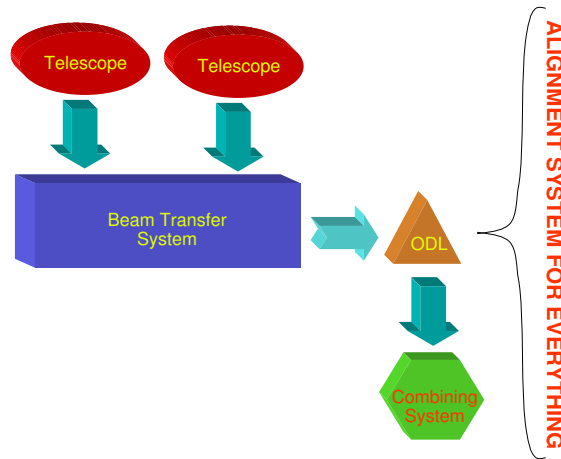


Figure 1.4: Schematic of an interferometer.



Figure 1.5: The Palomar Testbed Interferometer (PTI) delay line carriage

at a low cost. Once solved, the same solution may be used for the alignment sources and detector positioner. In order to achieve this aim, I considered a number of options to motorize the ODLs using available materials. Among various types of motors around, the simplest and most readily obtainable were stepper motors from precision equipment such as floppy disk drives. Driver cards were built for me to control the motors and a motorized ODL was tested in one arm of a Michelson Stellar Interfer-

ometer⁵ setup. The contents of the thesis is as follows:

Chapter 2: Historical Meanderings

A brief historical account through the technological developments applied to the construction of ground-based optical interferometers.

Chapter 3: Experimental Procedure

The experimental developments for the construction and implementation of the low cost ODLs.

Chapter 4: Results and Discussion

The results of this implementation, gauging the accuracy of this technique.

Chapter 5: Conclusion

This final chapter summarises and provides conclusions drawn from the work described in the thesis.

⁵This is an optical setup that we will discuss in Chapter 3.

Chapter 2

Historical Meanderings

Since prehistoric times, when gazing at the heavens, man has been confronted by an eternal question. What are the stars? We find throughout history that many notable names have tried to answer this, among them Galileo Galilei. We know of his most important practical achievement: building a telescope in 1609, which he used to observe the planets and to discover the moons of Jupiter, the mountains on the Moon and sunspots. He was also the first to notice the rings of Saturn. Galileo was the first person who tried to measure the size of stars. He tried to measure the star Vega's angular diameter using the well-known method of parallax¹. From this he concluded that Vega's diameter was less than 5" [4].

The first ideas of using interferometric methods to determine the angular size of the stars come from Armand-Hippolyte-Louis Fizeau[5]'s work in 1868.

¹Parallax is used in Astronomy to determine the distance to nearby stars. A star is observed from Earth once, then observed again six months later. The apparent angular displacement of star, caused by viewing it from different positions is the *parallax*. Using this angular displacement and trigonometry, the star's distance can be calculated.

Fizeau's work was entirely theoretical. Edouard Stephan[6], the director of Marseille Observatory, maintained written correspondence with Fizeau. In 1874, Stephan carried out the first attempt to determine interferometrically the angular size of the stars.

Stephan covered the opening of the Foucault² telescope with a mask in which he had previously perforated two holes diametrically opposed. The incident rays of stellar light passed through the openings, and converged to focus. A pattern of interleaved bright and dark bands was observed with an eyepiece. The bands appeared perpendicular to the straight line joining the centers of the mask's openings. These observations were carried out between 1872 and 1873.

Stephan was not able to resolve any star. But from these measurements he concluded (correctly) that the angular size³ of the stars had to be smaller than 0.15 arsec.

In 1891, using Stephan's technique, Albert Michelson[7] measured the angular diameters of the Galileans moons (the moons of Jupiter) using the 12 inch refractor at Lick Laboratory. But it was not until 1920 that Albert Michelson and Francis Pease, were able to use the new 100-inch telescope located on Mt. Wilson in California. They built a modified form of the Fizeau-Stephan interferometer, now

²The telescope that Stephan used was the largest reflecting telescope then in existence, with an entrance pupil diameter of 80 cm

³Angular resolution is given in radians by $\theta = 1.22 \frac{\lambda}{D}$, in this case $D=80$ cm and $\lambda = 550$ nm

known as the Michelson Stellar Interferometer. In principle it was similar but instead of using the circular apertures on a mask, two mirrors A and B were used to capture the starlight as shown in Figure 2.1. Initially these mirrors were 0.6 m apart. Then, once the light was picked up, it was directed towards two other mirrors C and D; those directed the light inside the body of the telescope towards the primary mirror.

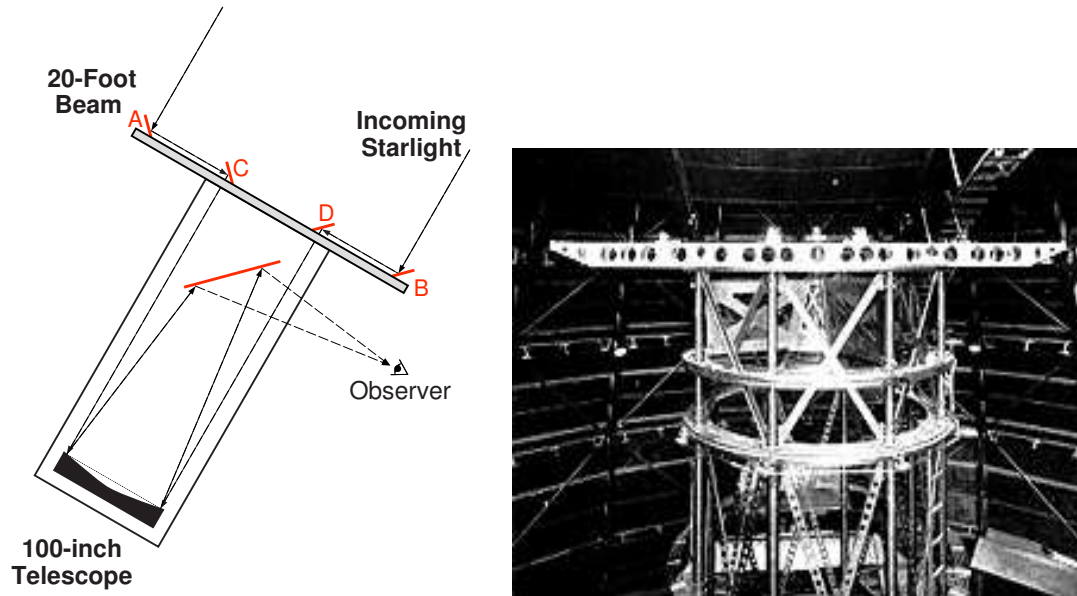


Figure 2.1: (left) Schematic diagram of 20-foot beam on top of the Hooker Telescope, (right) The 100-inch Hooker Telescope used by Michelson and Pease on Mt. Wilson in California.

Once the interferometer was built, they were able to measure the angular size of seven red giant stars[8] whose size varied between 20 and 47 mas⁴. It is interesting to notice that there exist strong clues that Michelson invented his interferometer without knowledge of the previous works of Fizeau and Stephan. One of

⁴mas means miliarcseconds

the arguments that are used to affirm this is that Michelson never made reference to the publications of Fizeau and Stephan. Further discussion may be found in the proceedings of the 1999 Michelson Summer School[16].

Leaving aside the unsuccessful attempts of Pease[9][10] to build a larger version of the Michelson Stellar Interferometer with baselines⁵ of the order of 1.5 m, interferometers of great size did not constitute an important tool in the Astronomy. This was due to the technological barrier of making mechanisms to track the atmospheric turbulence induced drifts of the interference fringes. The above-mentioned was in addition to the necessity of maintaining strict mechanical stability over such a large apparatus.

History takes us to Narrabri, Australia. Here, in 1963, Hanbury-Brown and Twiss built the Intensity Interferometer. This interferometer was able to measure the spatial correlations in the detected irradiance from two separate apertures. Contrary to the Michelson-Pease and Fizeau-Stephan interferometers, in this interferometer interference fringes are not formed. The theory of this technique is beyond the scope of this work and it is suggested to the reader that he refers to R. Hanbury Brown et al (1967)[11] for more details. Briefly, the Hanbury-Brown-Twiss interferometer had two light collectors of 6.7 m diameter shown in Figure 2.2, separated by distances

⁵Consider a model two-aperture interferometer, each one located at a three-space position \vec{x}_1 and \vec{x}_2 . Thus they are separated by a displacement $\vec{B} = \vec{x}_2 - \vec{x}_1$. \vec{B} is generally named the *baseline*

from 10 to 188 m. Using this novel instrument, Hanbury-Brown and J. Davis determined the angular size of 32 stars[12], which varied between 0.44 and 5.10 mas and whose magnitudes⁶ were above than 2.5. The arrival of the intensity interferometer attracted the interest of the astronomy community, giving a new impulse to optical stellar interferometry.

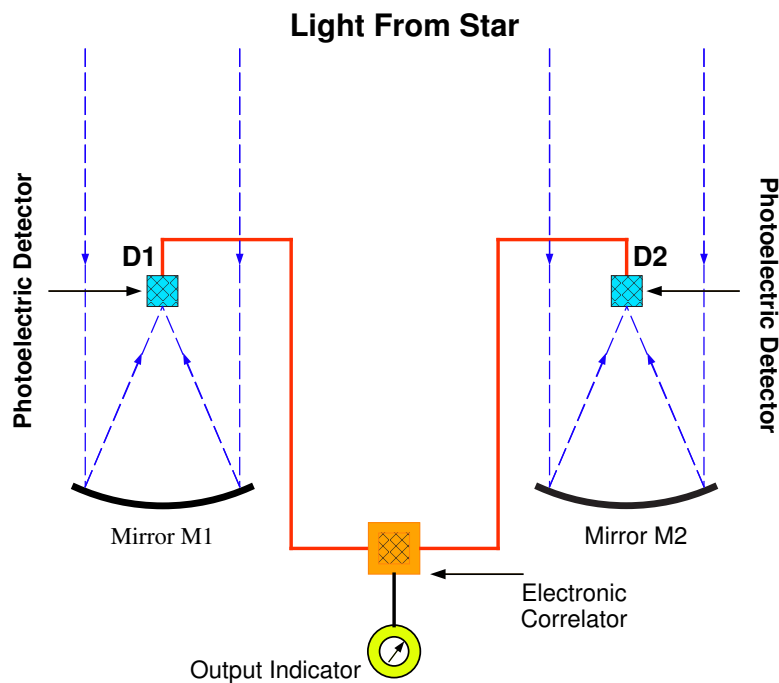


Figure 2.2: The arrangement of the Intensity Interferometer at Narrabri Observatory

Later on, the interferometers that were built recaptured the road traced by

Fizeau and Michelson. As for example, the I2T (Interféromètre à Deux Télescopes)

⁶The brightness class or *magnitude* can be defined in terms of the observed flux density F ($[F] = Wm^{-2}$). The magnitude of a sample star is given by $m = -2.5 \lg \frac{F}{F_0}$, where F_0 correspond to the 0 magnitude or 0^m . There are apparent and absolute magnitude; both depend on what wavelength or color is being observed. The absolute magnitude, M , is the magnitude of the object would have at a distance of 10 parsecs. 1 parsec=3.26 light-year.

of Antoine Labeyrie[13] in 1974 was the first to obtain interference fringes in infrared using two telescopes with baseline of 12 m. It could be said that the Modern Long-Baseline Interferometry born. After that, at the end of the 1970s and the 1980s other optical/near-infrared interferometers were built. The Mark I interferometer on Mount Wilson, built by M. Shao and colleagues, was the first one to track the fringe jitter in real time allowing long exposure times. The last in the series, the Mark III interferometer, the predecessor to the Navy Prototype Optical Interferometer (NPOI), was the most productive, although it was limited to stars brighter than fifteenth⁷ magnitude[14]; the Mark III measured the position of 11 stars with a precision of 10 mas, the diameters of about 70 stars more large that 2 mas, and the orbits of 26 binary stellar systems some smaller that 10 mas.

In the following figures two timelines are reproduced to illustrate the development of Optical Stellar Interferometry, obtained from the notes of the Michelson Summer School[16]. Each interferometer starts in the year it first acquired fringes and ends in its year of decomissioning. Milestones in the timeline are indicated by the triangles and described in the tables.

⁷In this case $\lambda = 0.4 - 0.9\mu m$, since magnitude depends on wavelength or color.

Year	Event	Authors and Reference
1868	Stellar Interferometry Suggested	H. Fizeau, C. R. Acad. Sci. 66 , 932 (1868)
1872-1873	Stellar diameters need be $\ll 0.158$ arcsec	E. Stephan, C. R. Acad. Sci. 78 , 1008 (1874)
1890	Mathematical theory of stellar interferometry	A. A. Michelson, Phil. Mag. 30 , 1 (1890)
1891	Satellites of Jupiter measured	A. A. Michelson, Nature 45 , 160 (1891)
1896	Binary stars measurements	K. Schwarzschild, Astr. Nachr. 139 , 3335 (1896)
1920	Orbit of Capella	J. A. Anderson, Astrophys. J. 51 , 263 (1920)
1921-1931	First stellar diameter measured	A. A. Michelson, F. G. Pease, Astrophys. J. 53 , 249 (1921)
1931-1938	50-ft. interferometer	F. G. Pease, Erg. Exact. Natur. 10 , 84 (1931)

Table 2.1: Events in Early Stellar Interferometry

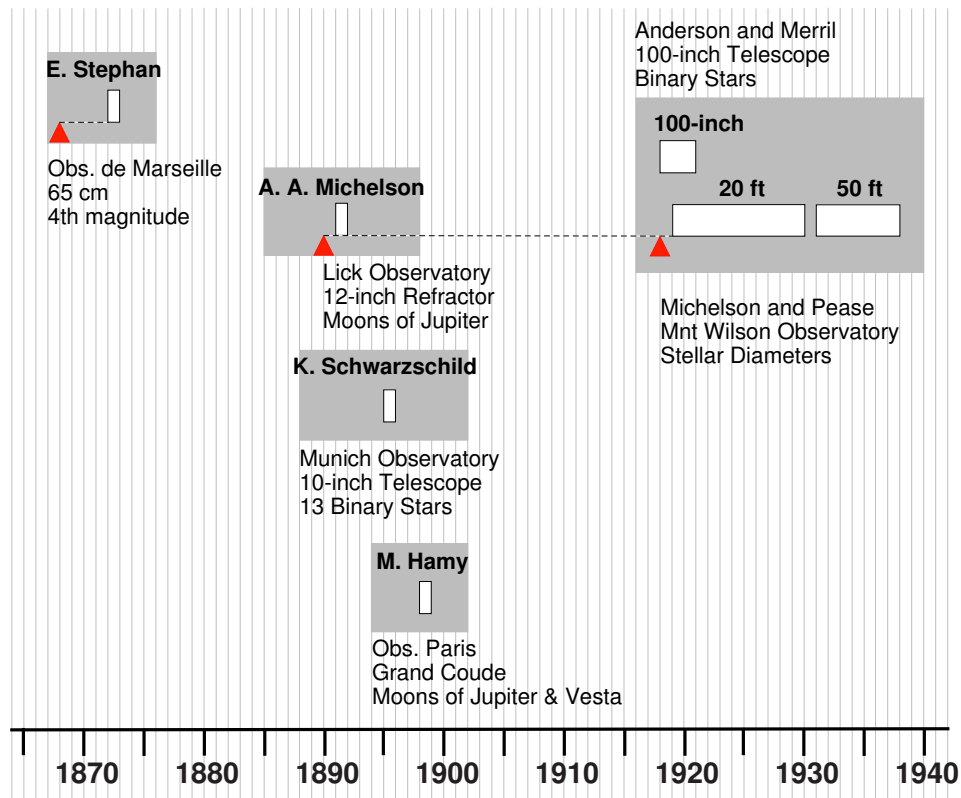


Figure 2.3: Timeline of Stellar Interferometry from 1868 to 1940

Year	Milestone	Authors and Reference
1956	Fringes with the prototype intensity interferometer	R. Hanbury Brown and R. Q. Twiss, Nature 177 , 27 (1956)
1970	Invention of speckle interferometry	A. Labeyrie, Astron. Astrophys. 6 , 85 (1970)
1972	10-micron heterodyne fringes	J. Gay and A. Journet, Nature Phys. Sci. 241 , 32 (1973)
1974	10-micron heterodyne fringes with separated telescopes	M. A. Johnson et al., Phys. Rev. Lett. 33 , 1617 (1974)
1974	Direct detection visible fringes with separated telescopes	A. Labeyrie, Astrophys. J. 196 , L71 (1975)
1979	Phase tracking stellar interferometer	M. Shao and D. H. Staelin, Appl. Opt. 19 , 1519 (1980)
1982	Fringe measurements at 2.2-micron	G. P. Di Benedetto and G. Conti, Astrophys. J. 268 , 309 (1983)
1985	Measurements of closure phase at optical wavelengths	J. E. Baldwin et al., Nature 320 , 595 (1986)
1986	Fully automated interferometer for astrometry	M. Shao, M. M. Colavita et al., Astron. Astrophys. 193 , 357 (1988)
1991	Use of single mode fiber with separated telescopes	V. Coude du Foresto and S. T. Ridgway, ESO Proc. 39 , 731 (1992)
1995	Optical synthesis imaging with separated telescopes	J. E. Baldwin et al., Astron. Astrophys. 306 , L13 (1996)

Table 2.2: Milestones in Long Baseline Stellar Interferometry

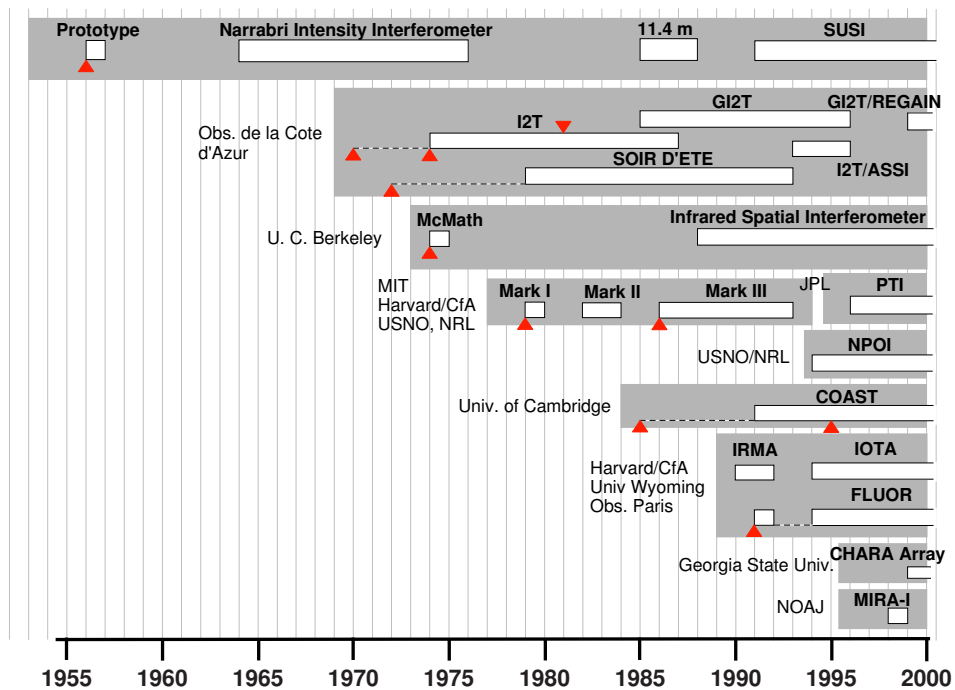


Figure 2.4: Stellar Interferometry from 1950 to 2000

Chapter 3

Experimental Setup

3.1 Principles of Optical Stellar Interferometry

A stellar interferometer (see Figure 3.1) consists of several light collecting elements (siderostats or telescopes) separated by a certain distance. The line separating each pair of elements is a baseline. Each element gathers a section of a wavefront that comes from a distant source. The two key factors in the operation of an interferometer are the system that equalize the Optical Path Lengths (OPLs) that the light waves traverse from the source to the combining plane, and the system that correlates the waves at the combining plane.

In Figure 3.1 we can see the schematic of a two-element interferometer. A_1 and A_2 are the two apertures, located at \vec{x}_1 and \vec{x}_2 respectively, where \vec{x}_1 and \vec{x}_2 are the position coordinates, in three dimensional space. So the baseline $\vec{B} = \vec{x}_2 - \vec{x}_1$. \vec{S} is the vector from the centerline of the array pair to the celestial source.

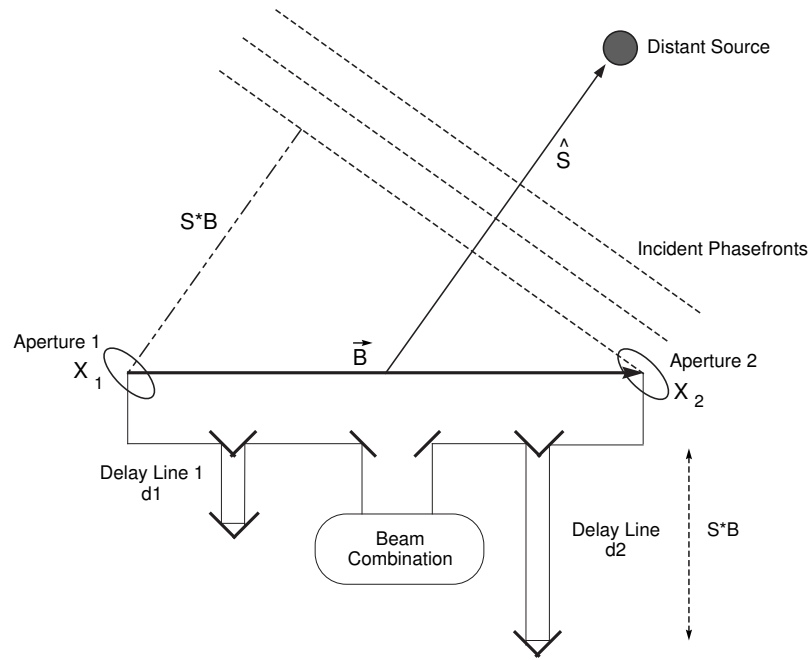


Figure 3.1: Schematic of a two-element stellar interferometer. S and B are vector quantities, and the source is infinitely far from the instrument.

The OPL traveled by each light beam includes the distance from the star to each telescope, through to relay optics, to the point where the light of the different telescopes is combined. The difference path in the lengths traveled between telescopes is denominated the *delay*.

With reference to Figure 3.1, the following three factors contribute to the delay in an interferometer:

Geometric Delay: this arises from the observed source being located nearer one telescope than the other, and is taken from the source to the telescope's entrance

pupils. In a stellar interferometer, this factor changes with the apparent rotation of the celestial sphere above the Earth.

Instrumental Delay: this is the difference in optical path length from the telescopes to the beam combination system.

Atmospheric Delay: this is due to the differences in the local refractive index across areas of each telescope pupil, caused by atmospheric turbulence, in the layers of air above the telescopes.

Geometric delay changes slowly, being a function of the Earth's rotation (the changes are of the order of hours), while atmospheric delay changes very quickly (the changes in the atmospheric turbulence are of the order of milliseconds). When the OPLs through each arm are the same, that is to say when the total delay is about zero, the waves interfere with the same phase, producing a pattern of fringes. To maintain a total delay near zero in the interferometer, the instrumental delay must be adjusted to compensate for the changes in the geometric and atmospheric delays. The amplitude of the fringes, their phases and positions, are used to produce an image of the source of stellar light and to measure its astrometric position¹ in the sky.

Almost all the current interferometers fulfill the adjustments of the instrumental delay using OPL compensators. Generally they include one per telescope in their interferometric array. These may be retroreflectors or a set of mirrors on carts

¹the astrometry is a method to determine the accurate relative position of stars on the sky.

that run on precision rails in the arms of the interferometer to modulate the instrumental delay for a few wavelengths, scanning (oscillating) at a few cycles per second to look for the interference fringes on the detector, and facilitating the detection of the fringes. In effect, the system attempts to track the fringe location by identifying the position of the group delay maximum. Another technique used is to follow the fringe drift as it moves, to try and keep it on the detector.

As for the combining system, the most common method of beam combination is to illuminate a beamsplitter with a ray entering each side of the beamsplitter. The two exit beams both contain the contributions of the entrance rays. The exit beams are then brought to detectors. This is referred to as pupil plane combination.

The aim of the work reported here is the construction and development of Optical Delay Lines² (ODLs) at a low-cost and to explore an alternative beam combining system to that of the pupil plane. The motivation to undertake image-plane interferometry (as Fizeau and Michelson did) is that, contrary to pupil-plane interferometry, a bigger field of view of the celestial source is obtained. Image-plane interferometry combines beams so each beam is focused to make an image of a portion of the sky. The images are superposed, so that interference fringes form across the combined image. The difference from this to pupil-plane beam combination is that

²A Optical Delay Line (ODL) is the device in the interferometer by means of the Optical Path Lengths (OPLs) of its arms are equalised.

at any one point in time, the pupil-plane is not capturing an image of the sky that is larger than a point. This means that we may detect more information simultaneously with an image-plane system.

The basic prototype laboratory based interferometer beam combiner that is planned is shown in Figure 3.2. Prior to its construction, a series of steps to build up necessary laboratory infrastructure and interferometer subsystems had to be accomplished. These steps are described in the following section.

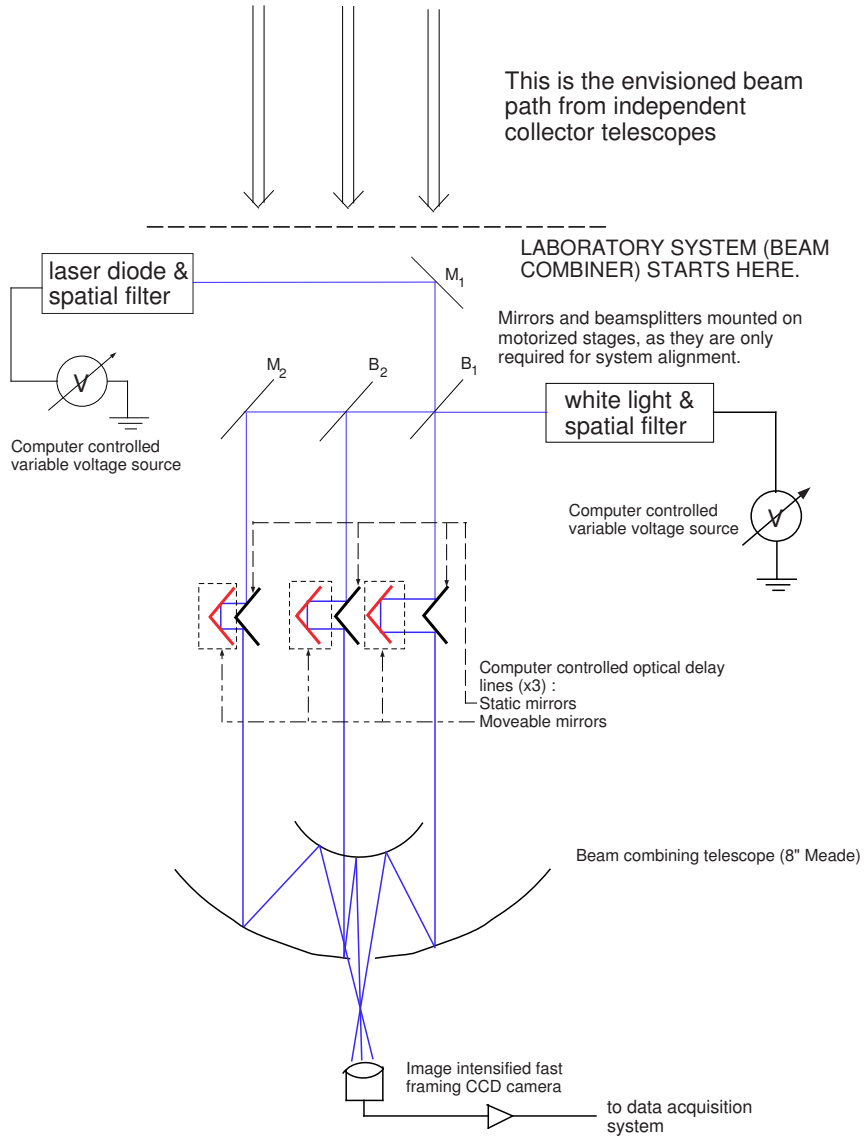


Figure 3.2: Schematic setup for the planned laboratory interferometer.

3.2 Electro–Mechanical Devices

In this section I describe all the related steps and resources used in the development of the aforementioned interferometer plan.

3.2.1 Creating the Ethernet and Computer Controllers

Keeping in mind the need to be able to control the system remotely, an Ethernet network³ was built within the laboratory⁴; this serves as the backbone of computer communications for the planned interferometer’s subsystem controllers, like the motorized ODLs to equalise the arms (see Figure 3.2), a set of artificial sources to align the interferometer optical components and detector positioning system(s) to ensure the fringes are brought into focus on the detection camera. The controllers themselves are Intel 386 and 486 PCs that have been reconstructed from decommissioned parts. These parts were acquired from the university’s physical plant. Two machines were built. One of them is a 386 PC with a 420 MB hard disk, 16 MB RAM, 3½” floppy and CD-ROM. A videocard was added and an EISA parallel port was found to work. An ISA network card was also recovered for each PC. The other processor is a 486 PC, with two hard disks (341.2 MB and 255.9 MB in master and slave configurations respectively); 3½” floppy, ISA videocard and network card and EISA, parallel and serial ports. They run a cut down version of Linux (Slackware 8.0) and are slaved

³An Ethernet is a type of LAN (Local Area Network).

⁴We lacked this resource in the lab.

to a master Pentium III, which was initially loaded with the Red Hat v7.1 Linux operating system. One other master PC running Windows was also required because software drivers for the video capture equipment (Matrox Meteor II) is not available under Linux.

3.2.2 Interferometer ODL Subsystems

From here onwards I discuss the subsystem details for building the Optical Delay Lines (ODLs). The aim of automating the system required finding suitable motors and building their driver circuits and relevant mounts.

Stepper Motor Implementation

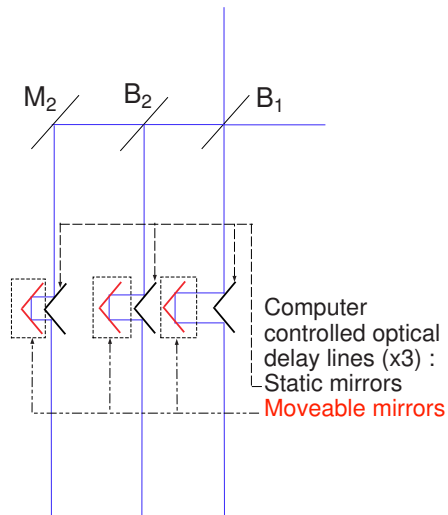


Figure 3.3: A detailed sketch of the ODLs planned in the Laboratory.

In order to motorise the subsystem that has been indicated in Figure 3.3,

the philosophy of “the simpler the better” was adopted. Therefore the plan was to control the motors through the parallel ports of one of the system control computers, which we recovered from the Physical Plant. The parallel port software interface is generally much easier to program than the serial port, which was the other alternative communications port. We considered making ISA or EISA controller cards to be inserted into the PC motherboards directly, but rejected the idea on the basis of cost and lack of relevant equipment.

Many older 5.25” floppy disk drives come with stepper motors as their workhorse motor. There are two type of stepper motor used to manage the floppy disk positioning for data input/output — unipolar and bipolar stepper motors.

There are many shapes and sizes of stepper motor. In order to understand how they work I dismantled the motors and using reversing engineering, can say that the motor type may be identified by inspection, as follows:

- A stepper motor with 5 wires is a 4-phase unipolar.
- A stepper motor with 6 wires is probably also 4-phase unipolar, but with two common wires. They may both be the same colour, if the wires are colour coded.
- A stepper motor with only 4 wires is most likely bipolar.

I chose to concentrate on the *unipolar stepper motor*, since this is the easier of the two types to use. An example of this is shown in Figure 3.4. Since some of the motors did not have colour coding, I used the following two techniques to identify the wires on this type of motor:

1. Isolate the common wire(s) by using an ohmmeter to check the resistances between pairs of wires. The wire will be the one with only half as much resistance between it and all the others. This is because the common wire only has one coil between it and each other wire, whereas each of the other wires have two coils between them. Hence half the resistance.
2. Identify the wires to the coils by supplying a voltage on the common wire(s) and keeping one of the other wires grounded while grounding each of the remaining three wires in turn and observing the results.

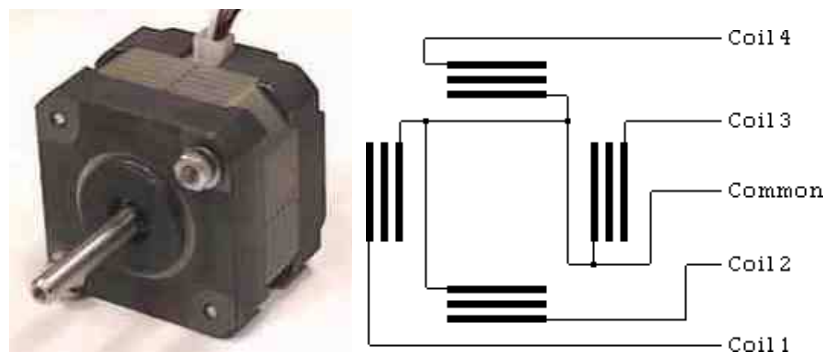


Figure 3.4: (left) A unipolar stepper motor from an old 5.25" floppy drives, (right) Schematic of the unipolar stepper motor coil layout.

A code using **C** language was written to control the stepper motors via the

control computer's parallel ports (see Appendix A).

With reference to the operation of stepper motors, there are two basic stepping sequences. Keeping in mind Figure 3.5, the normal operation is called **Single-coil Excitation** and visualized by the steps (1),(3),(5) and (7); after step (7) the sequence is repeated from step (1) again. With the stepper motors chosen, I found this method gave me steps of 3.6° axis rotation. Another operating sequence is **Two-coil Excitation**. This is schematically shown by (2),(4),(6) and (8) steps, so after step (8) the sequence is repeated from step (2) again. A combination of these two sequences gives us the sequence for the highest resolution linear stepping. Note that the two coil excitations require more power (and thus generate more heat) as well as producing more holding torque than just one coil. With the full sequence illustrated, resolutions of 1.8° per step is possible.

To understand what happens physically, let us go inside the stepper motor. The rotating shaft with permanent magnet attached is called the **rotor**. The stationary housing containing the 4-coil-wound poles is called the **stator**. With a unipolar motor, the current only flows in one direction in the windings of the coils, i.e. the stator poles can only be polarised one way.

In the stepper motor, the permanent magnet lies North - South along the

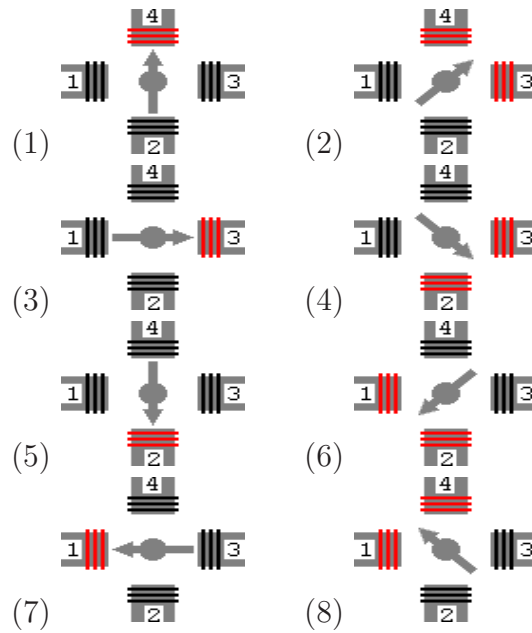


Figure 3.5: Stepping sequence. The simplest implementation, where only one pole is energised at a time follows steps 1,3,5,7. The more complex stepping sequence shown with all the illustrations gives twice as many stationary positions between steps as the simple sequence.

shaft. It is encased in two "stacks" each with 25 teeth round the rim. The teeth on the South stack are out of phase with the teeth on the North stack by half the gap between teeth.

This means that at the same time that the teeth on the North stack are being attracted by and thus lining up *with the teeth* on the currently magnetised pole of the stator, the teeth on the South stack are being repelled and thus lining up with *the gaps between the teeth* on that pole.

With 25 teeth round the edge of the rotor and 4 coils excited individually



Figure 3.6: The rotor of an unipolar stepper motor.

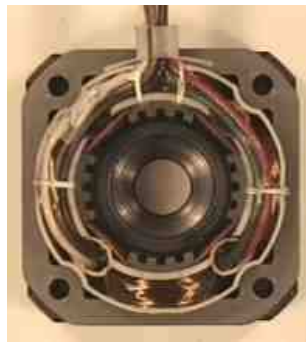


Figure 3.7: A stator of a unipolar stepper motor

in turn, the stepper motor takes 100 steps per complete revolution. The spacing between the teeth is $360^\circ / 25 = 14.4^\circ$. When the teeth on the rotor are aligned with the teeth on the stator pole of the currently excited coil, they are misaligned by a quarter of that angle with the teeth on the next stator pole (see Figure 3.8). So when the coil on that pole becomes energised instead, the rotor is pulled round through one quarter of 14.4° producing a step of 3.6° . So, the steps per complete revolution = Number of phases (coils) \times Number of teeth on rotor.

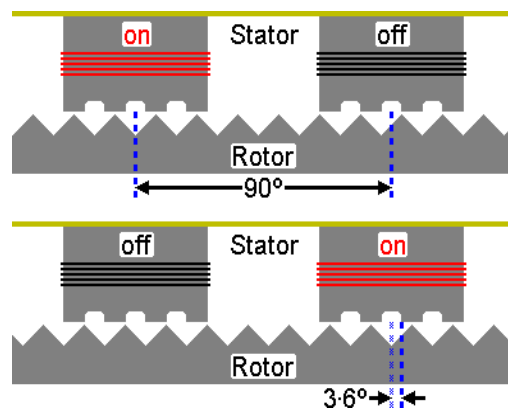


Figure 3.8: An explanatory sketch of the operation process of a unipolar stepper motor

Driver Card Construction

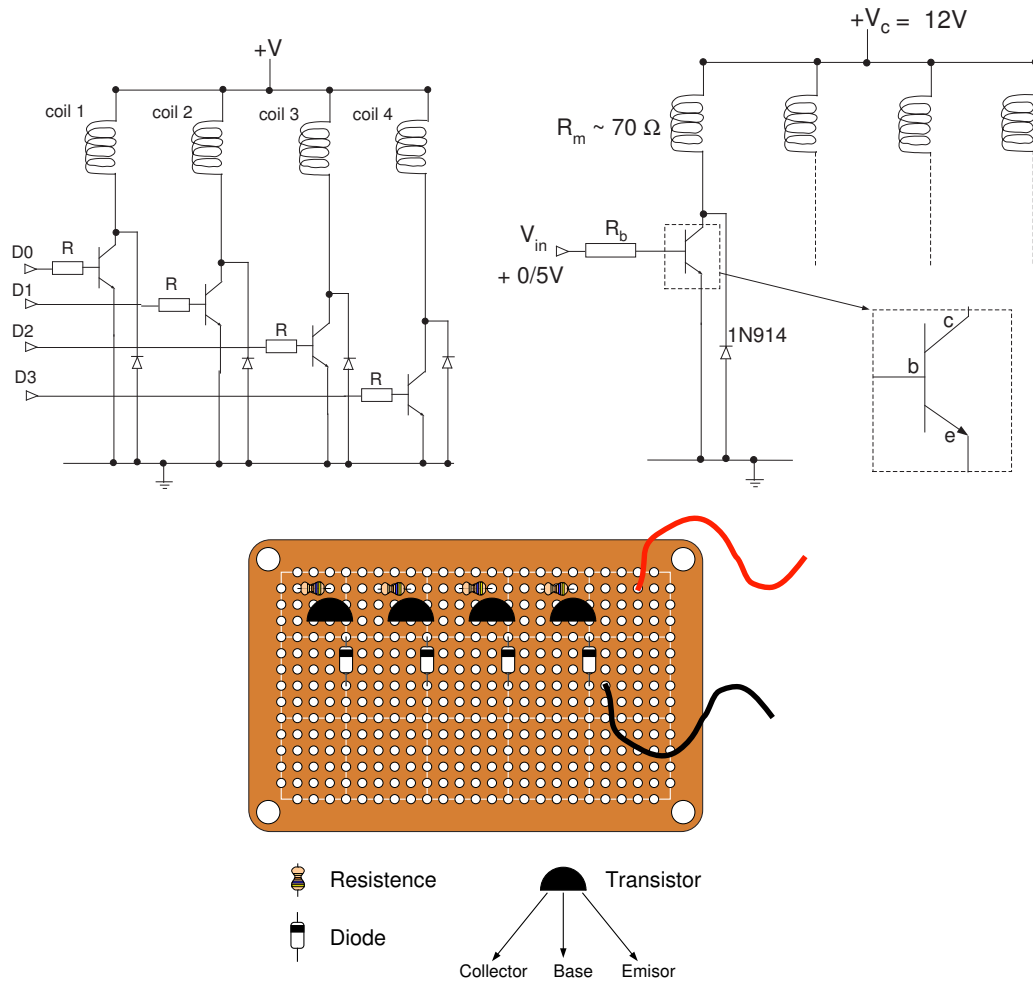


Figure 3.9: (a) A unipolar motor controller made from npn bipolar junction transistors (BJTs), (b) Detailed sketch from the unipolar motor controller, and (c) Drawing of the control card.

The electronic driver circuit for the uniphase stepper motors is shown in Figure 3.9. This is the simplest design of driver that I could use. The physical layout is also illustrated as can be seen in Figure 3.9(c). So, I mounted the electronic pieces. The circuit is designed so that each transistor acts as an electronic switch, controlling

a current that flows through the coils, from the collector to the emitter. This occurs only when a voltage is applied across the base resistor. A diode has been placed to absorb the induced back-*emf* which can occur upon powering down the coils. The coil resistances R_m were measured to be 75Ω . I have used 2N2222 npns since they are readily obtained. The diodes are commonly available 1N914s and the resistance values were obtained knowing that the transistor can handle a maximum collector current I_c of 800 mA. The input voltage V_c is +12V, which together with the coil resistance R_m and the maximum gain $h_{FE} = 10$ for this transistor type which results in an $I_c \lesssim 150\text{mA}$, well within the current limit of the device. The base resistor values were chosen to be 330Ω since the input voltages were anticipated to be no more than 5V, which is the general design voltage maximum for the parallel port, thus the base current is $I_b \leq \frac{5}{330} \sim \frac{1}{66} \sim 15\text{mA}$ (To see the calculation in detail, see the appendix C). The formulas used are:

$$V_{in} = I_b R_b \tag{3.1}$$

$$V_c = I_c R_m \tag{3.2}$$

$$I_c = I_b h_{FE} \tag{3.3}$$

Where,

V_{in} :	Base voltage
V_c :	Input voltage
h_{FE} :	The transistor gain
I_b :	Base current
I_c :	Collector current
R_m :	Coil resistance
R_b :	Base resistance

Figure 3.10 shows a schematic parallel port. The driver circuit for a single unipolar motor uses only four control pins per standard port. This means that we may simultaneously manage three unipolar motors with our design from a single port.

The original IBM-PC's Parallel Printer Port had a total of 12 digital outputs and 5 digital inputs accessed via 3 consecutive 8-bit ports in the processor's I/O space.

- 8 output pins accessed via the **DATA Port** (From D0 to D7).
- 5 input pins (one inverted) accessed via the **STATUS Port** (From S3 to S7).
- 4 output pins (three inverted indicated by the overbars) accessed via the **CONTROL Port** (from C0 to C3).
- The remaining 8 pins are grounded.

We can use pins D0 to D3, connecting a coil to each pin from one motor. The pins D4 to D7 and C0 to C3 can be used to connect to other two motors respectively. Applying a voltage through the pins allows us to activate each coil of the motors. When a pin is switched on it is represented by a binary 1 in software, and when it is off it is a binary 0. We must be aware that the pins C3, C1 and C0 are inverted, so these are activated by a binary 0 and deactivated by a binary 1 instead.

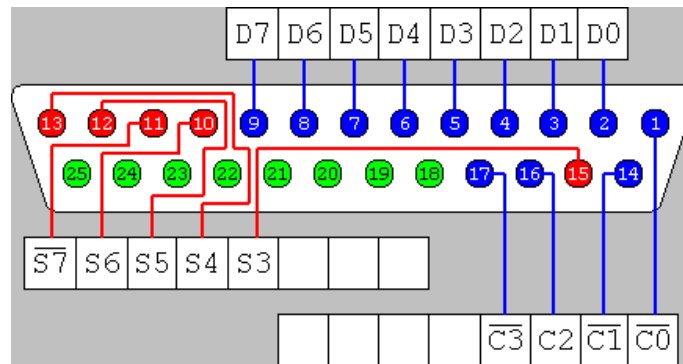


Figure 3.10: 25-way Female D-Type Connector.

Also standard PC architecture is designed in such a way that up to three parallel ports may be accessed from a single motherboard, giving even more flexibility.

Mount Calibration

To properly ensure the correct operation of the mechanism, a number of calibration measurements on a test rig were carried out. A control program was written in **C**. These were executed remotely by the master computer to run the stepper mo-

tors through the parallel port of a slave. Figure 3.11 shows the calibration mount controlled by a stepper motor. This was chosen to be representative of the weight carried by each stepper motor. The physical drive shaft of the test stepper motor was connected to a pulley by a small rubber belt. These belts are the type used in VCRs and cassette recorders. The pulley itself was mounted on a micrometer screw drive, designed to push a single-axis optics mount.

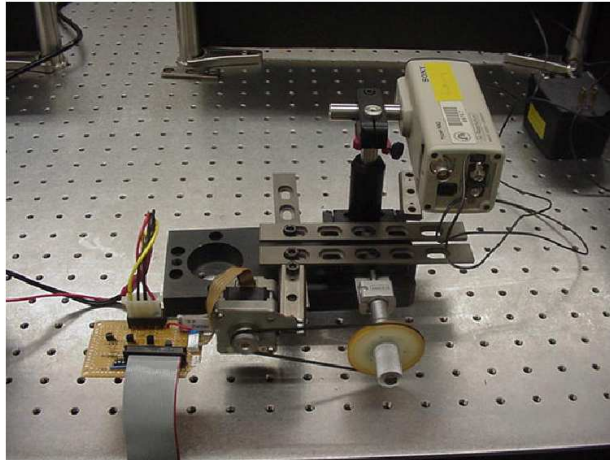


Figure 3.11: Unipolar stepper motor calibration mount.

To test the possibility of having multiple parallel ports in a slave computer,

I inserted 3 parallel port ISA cards in one of the slaves. A simple test circuit based on LEDs and resistors was designed and several were constructed in order to determine the independence of the parallel ports. Each circuit consisted of LEDs connected to the pins that were to be used to drive the motor, plus a resistance down to ground. One circuit per parallel port was connected. Figure 3.12 illustrates the test circuit which was used to probe each line. One boot-time command was changed in the Linux system file, */etc/modules.conf* as follows, in order to have the multiple parallel ports recognized:

```
options parport_pc io=0x378,0x278,0x3bc irq=none,none,none
```

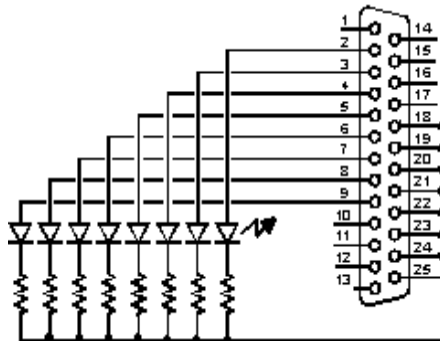


Figure 3.12: Schematic circuit to test the parallel port independence.

3.3 Basic Interferometer

Before starting with the construction of the interferometer, we decide to do some simulations to understand the differences between the functionality of a tele-

scope and an interferometer. We wanted to study our detector's response to potential (but simulated) observations. To do this we used the Matlab programming environment; also this was motivated by the idea to use Matlab as the general data analysis tool for the interferometer.

3.3.1 Qualitative Simulations of an Interferometer

I began with a script to simulate what we would obtain with an ideal detector in the image-plane when a plane wavefront (signal) was incident on a circular aperture in the far field regime (Fraunhofer Diffraction). The script was developed for 1D and 2D space. The script carries out a Fourier Transform (FT) of the signal. Why an FT? Let $A(y)$ be the Amplitude Transmission Coefficient for a finite aperture illuminated by a plane wave (see Figure 3.13).

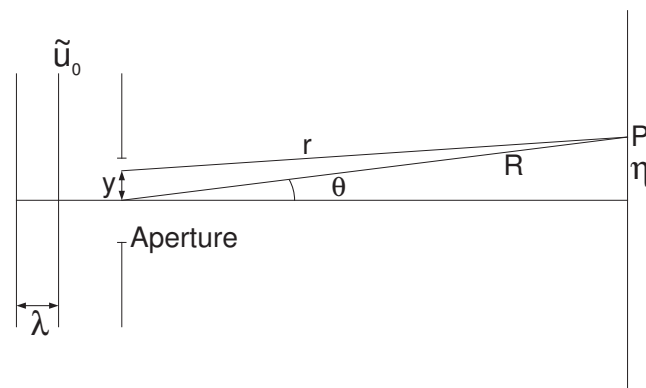


Figure 3.13: Plane wave incident on a finite aperture.

If \tilde{u}_0 is the initial amplitude, then $\tilde{u}_0 A(y)dy$ is the transmitted amplitude through dy the aperture, originating at a point. So, using Huygen's model of light propagation, the amplitude seen at the observing plane P due to the point dy in the aperture is

$$d\tilde{u}_p = \frac{\tilde{u}_0}{r} A(y) e^{-ikr} dy \quad (3.4)$$

thus the total wave at P is the integral over the full aperture

$$\tilde{u}_p = \int_{\text{aperture}} \frac{\tilde{u}_0}{r} A(y) e^{-ikr} dy \quad (3.5)$$

$$\text{If } y \ll r \text{ then } \begin{cases} r \approx R - y \sin \theta & \text{in } e^{-ikr} \\ r \approx R & \text{in denominator} \end{cases} \quad (3.6)$$

Taking into account that $k = \frac{2\pi}{\lambda}$ and the equation 3.6

$$\tilde{u}_p = \left\{ \frac{\tilde{u}_0}{R} e^{-ikR} \right\} \int_{\text{aperture}} \mathcal{A}(y) e^{iky \sin \theta} dy \quad (3.7)$$

Let $u = \frac{\sin \theta}{\lambda}$, this implies that the aperture has finite size, and if we assume that

$\mathbb{C} = \frac{\tilde{u}_0}{R} e^{-ikR}$, is a constant value, then

$$\tilde{u}_p = \mathbb{C} \int_{-\infty}^{\infty} \mathcal{A}(y) e^{2\pi i u y} dy \quad (3.8)$$

So, $\tilde{u}_p = \mathcal{F}^{-1}(\mathcal{A}(y))$ which is a inverse Fourier Transform (FT) of the transmission function. However, both in this simulation and in the final measurements we do not have continuous functions. We have instead functions given at discrete values. So in such cases we deal with Discrete Fourier Transforms (DFTs) over physical measurements. The most well known set of methods to rapidly compute the DFT of a set of data are referred to collectively as the Fast Fourier Transforms (FFTs). Two scripts were elaborated (in 1-D and 2-D), simulating a signal and its corresponding FT (See Appendix B).

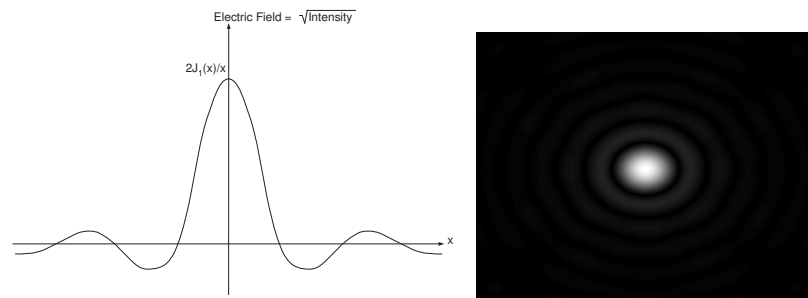


Figure 3.14: (left) Electric field function of the radial amplitude distribution in the diffraction pattern of a circular aperture, (right) Electric field diffraction of a circular hole simulated with the Matlab script. Note that it is the square of this function that is detected and not this function directly.

Well, the visual description offered by Matlab is appropriate to understand the optical physics in the telescope. But, what we will see in an interferometer? Using

Matlab again, we simulate a two aperture interferometer as can be seen in the Figure 3.15, and to see how two apertures works.

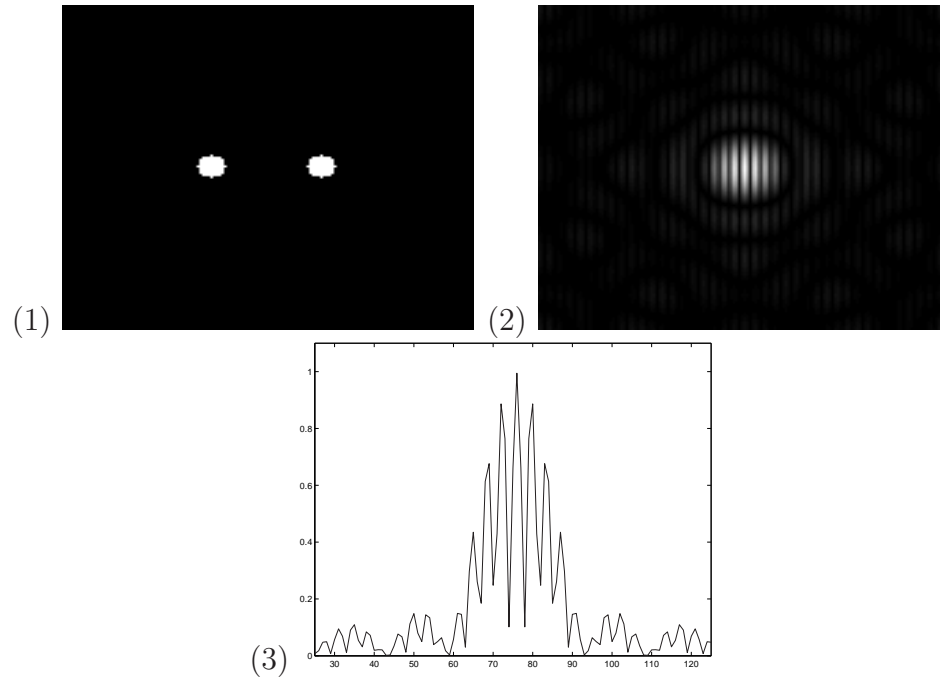


Figure 3.15: (1) Mask with two holes (apertures); (2) interference pattern simulated where we can see the fringes; (3) profile of the interference pattern.

Note in the profile that although the fringes are observed, there is an envelope function that contains the fringes. This is a function of each aperture geometry, in this case is due to the circular apertures. The fringe separation is a function of the separation of the apertures. Now, what will occur when the signal through each aperture arrives with a different phase? In our simulation we take one aperture and multiply the function by a phase factor; we are expecting that the high contrast fringes (zero delay position) will be affected in their position as shown in Figure 3.16. If we

apply an increasing phase factor in time, then all fringes will be observed moving; as we may expect when an ODL is moving to compensate the optical path difference. For the following sequence the phase factor is $e^{2\pi in}$ where $n=1,2,3,4,5$ for (1), (2), (3), (4) and (5) respectively.

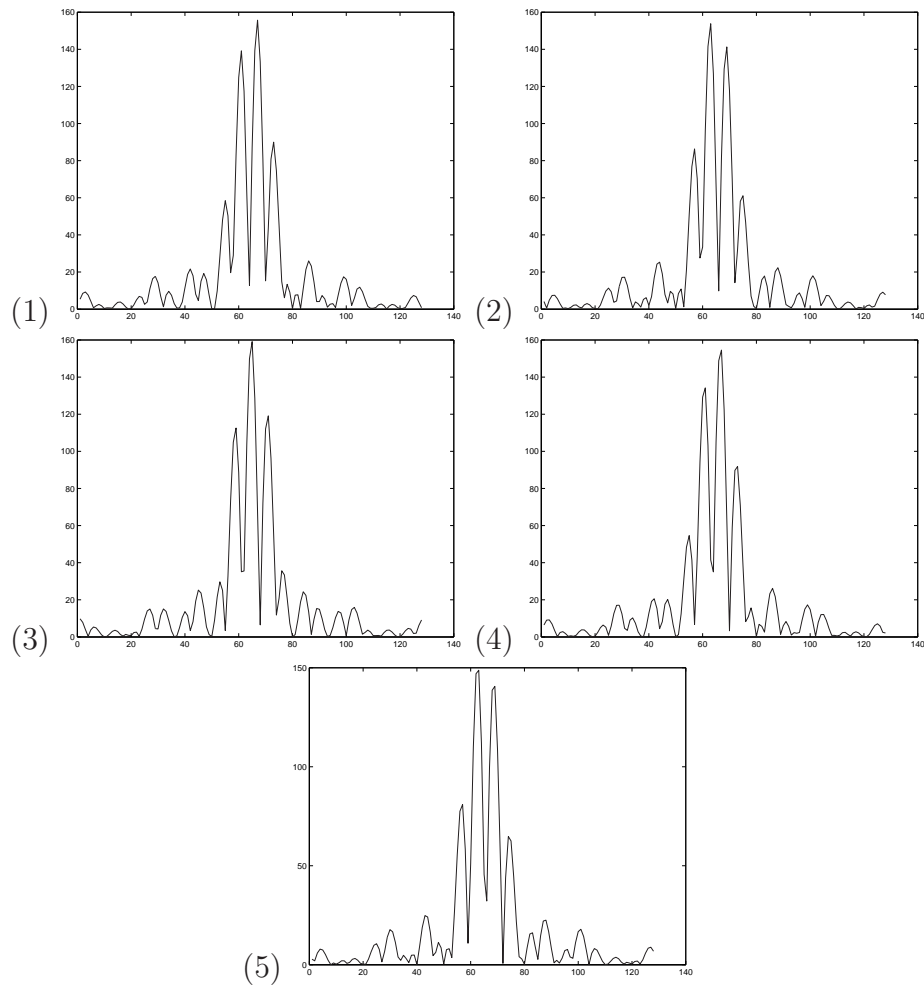


Figure 3.16: Sequence showing the movement of the fringes (showed as cross sections) when a phase factor is applied in one of the apertures. The displacement is toward right side.

After the simulations and having the stepper motor systems for driving the mechanical stages of the interferometer, I decided to build the interferometer in small steps of increasing complexity. Subsequently, each step is explained briefly and will be enlarged in a later section.

Michelson-Morley Interferometer geometry: This was necessary to study the temporal coherence⁵ of the laser light, because the visibility of the interference pattern is a measure of the coherence of the light.

Direct Two Beam Interferometer: The two perpendicular beams are directed from the beamsplitter in the Michelson-Morley setup towards an 8" telescope, where they are combined at focus. This means that one of the beams had to be folded by 90°, introducing a path difference between the beamsplitter and the fold mirror. The main restriction found was that the Optical Path Difference had to be inside the coherence length of the laser⁶. This interferometer geometry still lacked the internal, mechanized ODLs to compensate for the optical delay due to geometrical path differences.

Michelson Stellar Interferometer: Finally, a version of Michelson Stellar Interferometer was built where an automated ODL is implemented in one of the arms.

⁵The time for which the phase is constant during the emission of a source that emits in a range of wavelengths.

⁶In order to obtain fringes of good visibility. This is the reason for the ODLs.

3.3.2 Michelson-Morley Interferometer Setup Study

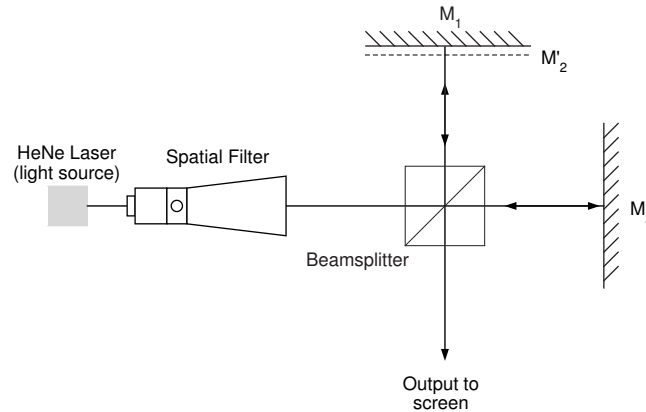


Figure 3.17: Michelson-Morley Interferometer setup

A Michelson-Morley Interferometer was built so that I could understand the source characteristic effects, namely spatial and temporal coherence, on the interference fringe signal. The setup is shown in Figure 3.17. It consists of two mirrors M_1 , M_2 and a non-polarising cube beamsplitter which is a transparent element with a diagonal interface that partially reflects and transmits the incident light. The light source used was a HeNe Laser ($\lambda = 632 \text{ nm}$) that was divided in two perpendicular beams upon going through the beamsplitter. The rays are reflected at the mirrors M_1 and M_2 . Let M'_2 be the virtual image of M_2 formed by reflection in the beamsplitter. We can visualize the interference of the two rays of light coming from the reflected images of the mirrors M_1 and M_2 . It is necessary to use a laser, because this guarantees that the interference fringes will be observed. Why a laser? To produce perfect interference we need the wave from one arm to be in phase with all points of the wave

of any other point of the wavefront of the other arm that goes through the optical system at any instant in time. This is called coherence and the laser is an example of coherent light to a very good approximation. It is convenient to clarify that the concept of a monochromatic point source is a mathematical idealization. Realistically, the best approximation of a monochromatic source is one that emits a narrow range of wavelengths (i.e. laser). So we can imagine the emission as being made up of finite wavetrains instead of a single frequency sine wave of infinite extension. The time during which the phase difference stays constant within the wavetrains is called the coherence time Δt . The corresponding spatial interval $\Delta l = c\Delta t$ is the coherence length. For the laser, the coherence length is related with the length of the gain medium.

We should equally consider that the laser is an optical resonator, so vibrations also exist in the plane normal to the direction of propagation of the light. These transverse vibration modes travel with different speeds and respond differently to system perturbations. This means that the beam will appear “dirty” if it is merely expanded. To remove the contribution of the non-fundamental vibrations (high frequencies) we use a spatial filter. This allows us to “clean” the beam profile. An outline of the spatial filter can be seen in Figure 3.18.

If we do not use a laser, we have to use a point source. Then the inter-

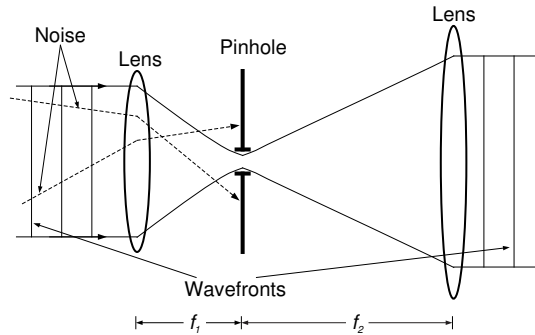


Figure 3.18: Spatial filter sketch

ference fringes can be seen in any region where the rays of light are superimposed. Using an extended source, interference fringes of good contrast are observed only in a particular region; this phenomenon is known as localized fringes and it is related, in particular, with the coherence of the source of light. A source of finite size can be considered as being constituted of an arrangement of independent point sources, each pair of which reproduces a separate interference pattern. If the difference in the OPLs at the observation point is not the same than those of the waves originating from different points of the source, these interference patterns will not coincide and when they are superimposed, an interference pattern of low visibility or contrast will be observable. Figure 3.19 illustrates the instrumentation and the fringes obtained in the Michelson-Morley Interferometer.

An experiment was carried out to study, qualitatively, the fall of the visibility of the fringes when the distance between the beamsplitter and the mirror M_2 was varied. This distance was varying with increments of 1 inch. I observed that the

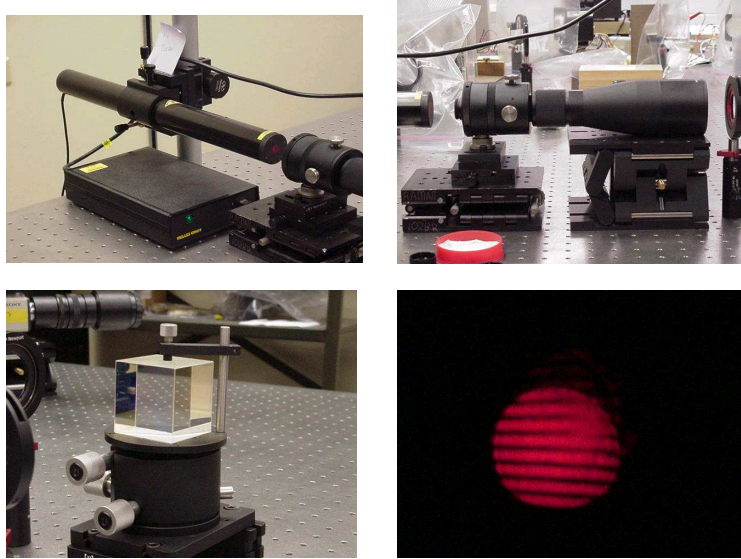


Figure 3.19: (top left) The HeNe laser used in the Michelson-Morley Interferometer; (top right) spatial filter; (below left) beamsplitter used; (below right) the fringes obtained are quite visible.

visibility of the fringes diminished until near 0 when the OPD (difference between the arms) of the interferometer was approximately the length of the laser tube, which is sketched in Figure 3.20. This plot is very similar to the sinc ($\text{sinc}(x) = \sin(x)/x$) function. Since the visibility function is a FT of the source frequency spectrum, the laser is not a true monochromatic source.

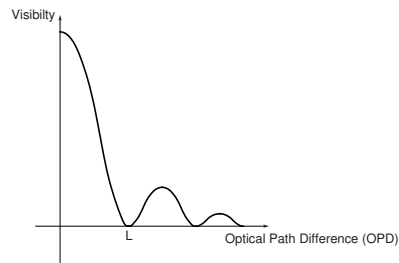


Figure 3.20: Visibility versus the optical path difference between the arms.

3.3.3 Two Direct Beam Interferometer at Focal Plane

After building the Michelson-Morley Interferometer the next step to continue our work consisted of modifying this setup slightly to prepare a new setup that would introduce two beams into a Schmidt-Cassegrain telescope. This combiner telescope is 8-inch diameter, and will combine the light beams in its focal plane. To do this we use a beamsplitter on the single beam coming from the laser, to split in two beams, one which passes directly to the telescope through the beamsplitter; the other ray is redirected, using a mirror M_2 as can be seen in Figure 3.21. This simulates the light gathered through two hypothetical collector telescopes from a single star. There are two key aspects in this setup: the first is that the rays going toward the telescope should maintain high parallelism. Should this not be obeyed, the rays will be introduced with different angles with respect to the telescope and each will have a different focal point. The second aspect is that the distance of the beamsplitter to the mirror M_2 should be smaller than the coherence length of the source for good conditions of visibility, because, the visibility of the fringes is a function of the coherence of the light as seen with the Michelson-Morley experiment. If these conditions are not fulfilled then it is very probable that interference fringes are not observed, or will be of very low visibility. To ensure parallelism of the beams within Figure 3.21, I aligned the beams from the beamsplitter following the recipe described below:

1. The beams that were transmitted and reflected by the beamsplitter were returned by aligning mirror M_2 at a perpendicular angle to the incident beam

and by introducing a new mirror M_4 , in the transmitted arm, again perpendicular to the incident beam. This formed a standard Michelson-Morley, giving high visibility fringes when the components M_2 , M_3 and the beamsplitter are properly aligned.

2. I then set M_2 at a 45° angle to the incident beam, directing the light to the combiner telescope. I moved M_3 downstream, placing it halfway between the combining telescope and the beamsplitter. Another mirror M_4 was placed in the beam from M_2 , reflecting the light back to M_2 . This allowed me to adjust the alignment of M_2 by finding the fringes.

Regarding the second key point, we were careful to keep the distance between the beamsplitter and the mirror M_2 within the coherence length of the laser in order to obtain the best visibility of the fringes.

3.3.4 Michelson Stellar Interferometer

There are no significant differences between this arrangement and the previous one. The distance from the beamsplitter to the mirror M_2 was increased, although still maintained inside the range of the coherence length of the laser. The same procedure was done to conserve the parallelism of the beams from the beamsplitter and the mirror M_2 up to the mirrors M_4 and M_3 respectively. As we see in Figure 3.22, two mirrors have been introduced M_5 and M_6 to direct the beams inside the telescope.

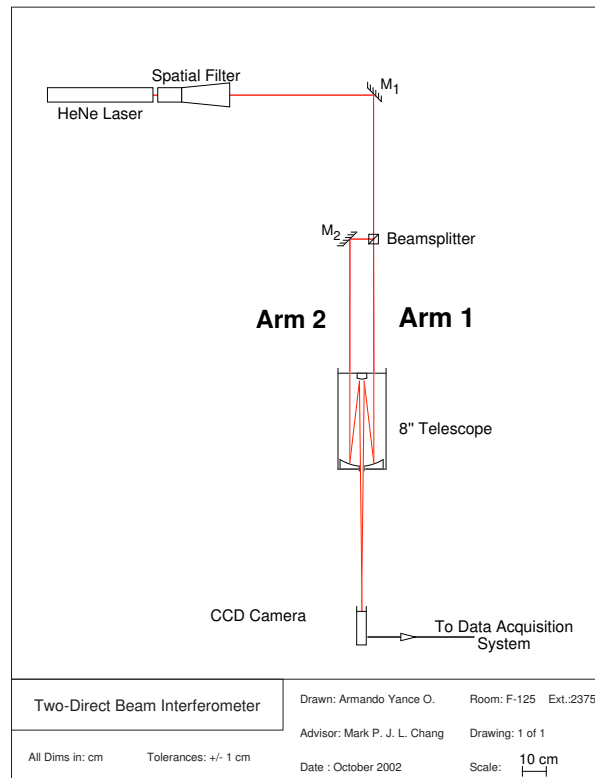


Figure 3.21: Schematic of Two Beam Interferometer.

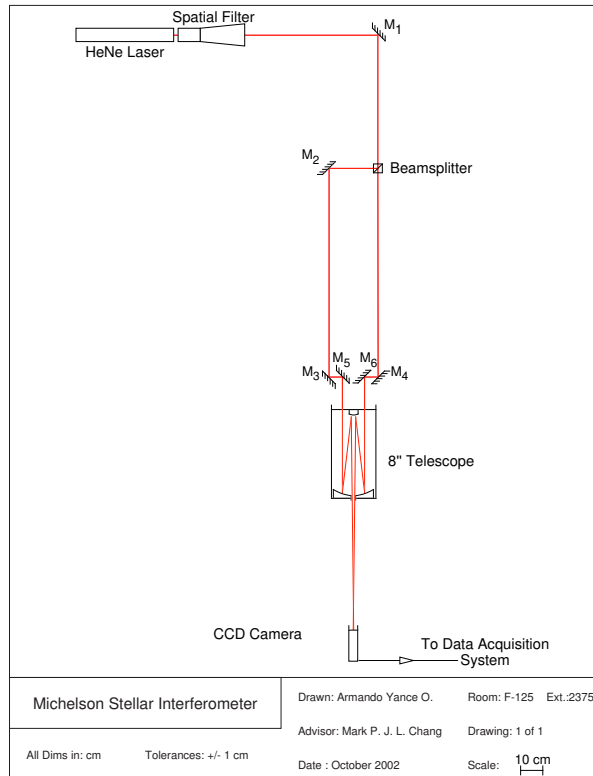


Figure 3.22: Schematic Michelson Stellar Interferometer.

Later an ODL was added in one of the arms (right arm, the mirrors M_7 , M_8 , M_9 and M_{10}) of this interferometer (see Figure 3.23) to compensate for the resulting geometric delay; which is the additional path between the beamsplitter and the mirror M_2 in the left arm. Four mirrors were placed to interrupt the path of the beam that runs from the beamsplitter towards the mirror M_4 . Two were fixed (M_7 , M_{10}) and the other two, M_8 and M_9 , can move by means of a micrometer screw drive. This drive is the parallel port controlled stepper motor system described in section 3.2.3. To capture the images in all the setups described, I used a Sony Hyper HAD Hi Resolution

B&W video camera with a Rodenstock zoom lens. The data obtained as well as the analysis for the fringe visibilities in the experiments will be found in the next chapter.

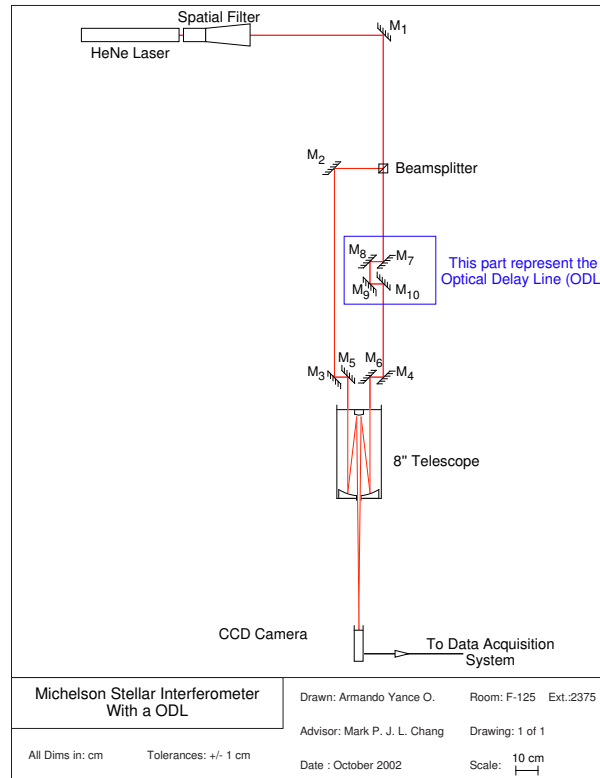


Figure 3.23: Schematic Michelson Stellar Interferometer with a ODL.

A calibration process was undertaken to determine the errors in lateral displacements and the precision of the setup of the ODL. For every five steps of the stepper motor, an image of the fringes was taken to determine the ODL displacement.

Chapter 4

Results and Discussion

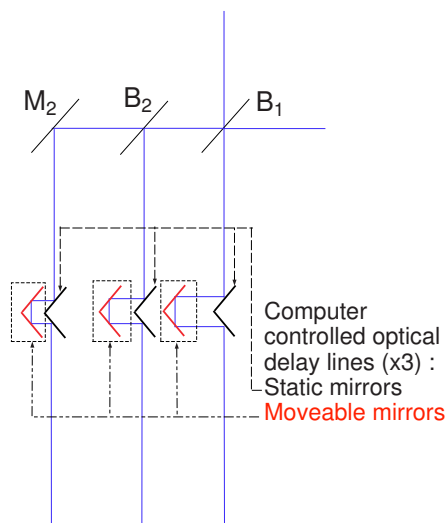


Figure 4.1: Detail from the ODLs planned in the Laboratory.

As stated in Chapter 3, the first steps to build an ODL in one of the arms of the interferometer was the implementation of a stepper motor to control the movement of the two mirrors, those which constituted the ODL (See Figure 4.1). Three recycled motors were used, each one connected to a custom built driver card. These were tested to demonstrate the features of the control system based on the

parallel port of a standard architecture PCs, and we proceeded to calibrate each motor. Also, the stability of Linux like operating system was good. The PCs was running Linux for many hours without any crash. Our interest was:

1. Verifying the linear response of each motor when moving in one direction. This is also a measure of the linearity of the screwthread.
2. Investigate if the linearity was maintained when the motor was displaced in one direction by a certain number of steps and then returned by the same numbers of step. In other words, this is a measure of the displacement error due to the backlash effect in the micrometer screw.

Figure 4.2, shows the displacement variation against number of steps moved by the motor. The lapse (delay) between steps, was varied taking 10 ms, 1 ms and 0.1 ms for the first motor (see Appendix D for the complete information of the calibration plots). The objective was to check the hysteresis existence in the motors, to prove that they were not damaged (remember that this is decommissioned equipment). It was proven that they did not have hysteresis. Variations in the linearity of the motor displacement due to change in delay between steps were not observed. We conclude that the displacements were independent of the time between steps.

We set 1 ms of delay between steps for all motors, before carrying the calibration measures. After, we proceeded to move the ODL mount changing the number of steps executed by the motor in one direction and reading on the micrometer screw

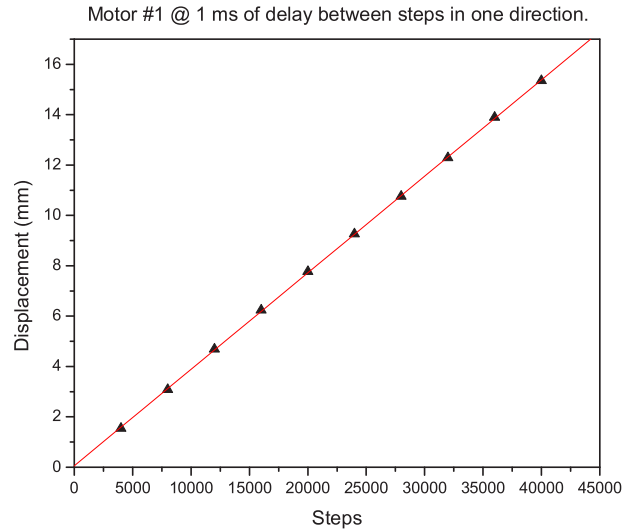


Figure 4.2: Graph of the calibration data for the stepper motor #1 in one direction @ 1ms of delay between steps.

the displacement in mm. Ten data points were taken as shown in Figure 4.2. For each data, the corresponding resolution in terms of millimeters per step was calculated. For example, in the first dataset, 4000 steps made by the motor correspond a length traveled by the ODL of 1.56 mm. Since the ODL traveled 390 nm per step with an error of 0.5%, this shows the linearity of the motor is high. For the second motor the sweep was of 410 nm per step and an error of 0.2%; and the third motor traveled at 400 nm and had an error of 0.2%. For the bidirectional sweeps the calibration measurements were less accurate as can be seen in Figure 4.3. the bidirectional sweeps that the calibration mount carried out was moving in one direction a certain number of steps and later to return in the contrary direction the same numbers of steps. It was expected that the difference between the initial position and the final, due to

the backlash effect in the micrometer screw and belt slippage around the rotor of the motor, was small or there is a linear dependence between the steps executed by the motor and the displacement. The same as with the calibration in one direction, the numbers of steps was the independent variable and for each change of this variable, the distance between the initial position and the final was measured. We finds that for the bidirectional sweeps there was no linearity (see Figure 4.3), the measurements fluctuated between a range of 0.02 mm to 0.16 mm. So, we have a limit of displacements from the original position for each motor. For the motor #1 the upper limit was 0.16 mm; for the second motor was 0.11 mm and in the third motor case was of 0.055 mm.

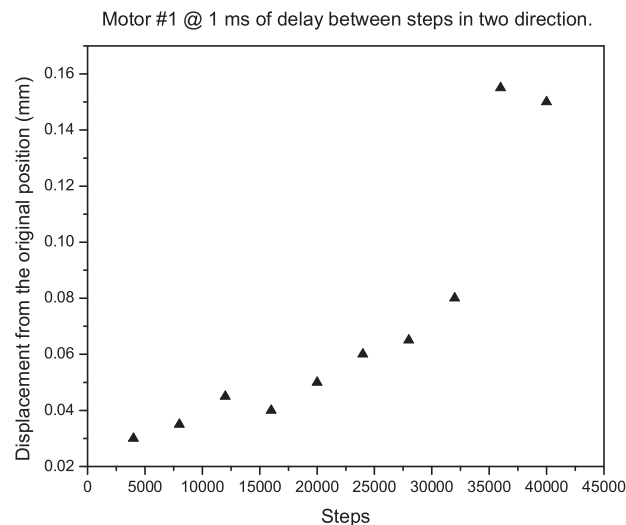


Figure 4.3: Calibration graph for the stepper motor #1 in two direction @ 1ms of delay between steps.

If we extrapolate this measure to a situation where the ODL carries out oscillations around a specific point; then for example the first motor makes ten oscillations and if we assume that the effect due to the bidirectional sweeps is cumulative, in other words the upper limit is added to the others, we have a total displacement from the original position of ten times the upper limit ($10 \times 0.16 \text{ mm} = 1.6 \text{ mm} !$). So, this error is too large to be neglected.

Now, with respect to the interferometers setups we wanted to study the fringe contrast or visibility¹. Three images were taken for each setup, one of them without and the other two with a polarising filter of alternated vertical and horizontal orientation with respect to the optical table. Why polarizer filters? Because we want to know qualitatively if there was a preference in terms of polarizations states s and p (s=senkrecht and p=paralel, that means perpendicular at interface(s) and parallel at interface(p)), due to the reflections on the mirrors². As is shown in Figure 4.4 the fringes from the Two Beam Interferometer with and without the polarizer filter. From the images, we can see that the polarizer filter improves the signal-to-noise of the fringes even though it diminishes the throughput. Other images including those from the Michelson Stellar Interferometer are shown in Appendix D. A Matlab script was designed to extract the visibility information from the fringe patterns. The

¹Fringe contrast or Visibility is defined as $V = \frac{I_{max} - I_{min}}{I_{max} + I_{min}}$ where I_{max} , I_{min} represent the maximum and minimum intensity values respectively

²when the light is refelected in a surface can be polarized with respect to the plane of reflection, this effect (known as polarization by reflection) depends of the incident angle. To a upper angle, the polarization will be bigger.

fringes from the Michelson Stellar Interferometer with an ODL (which I will call the Michelson Compensator from here onwards) presented a difference which consisted in an off-vertical orientation. To overcome this, a smaller function was added to the program to rotate the image as can be seen in Figure 4.5.

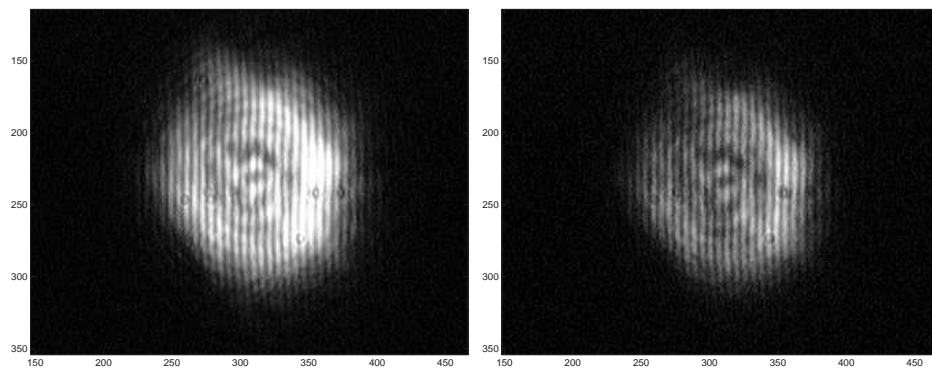


Figure 4.4: (left) First fringes obtained from Direct Two beam Interferometer without polarizer, (right) the same setup but using a vertically aligned polarizer filter.

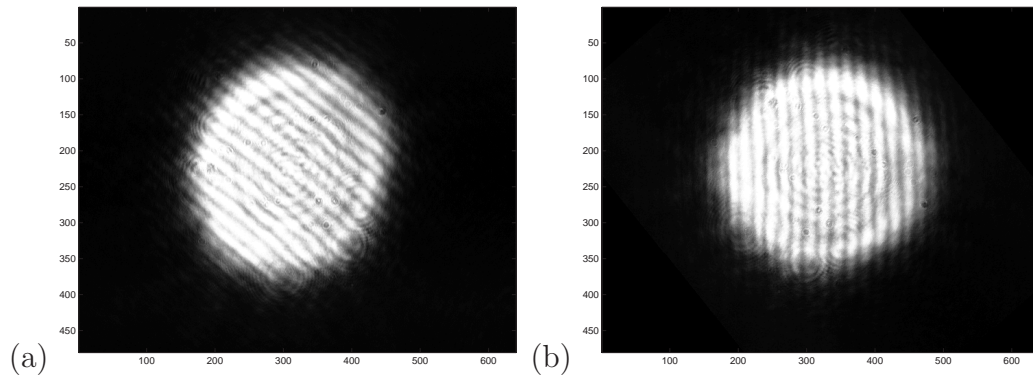


Figure 4.5: Fringes obtained from Michelson Stellar Interferometer with ODL. (a) Original image, (b) Image rotated.

With relation to the images in two dimensions, the horizontal and vertical axis only represents the pixels of the CCD sensor in the camera. We can find a 3-D

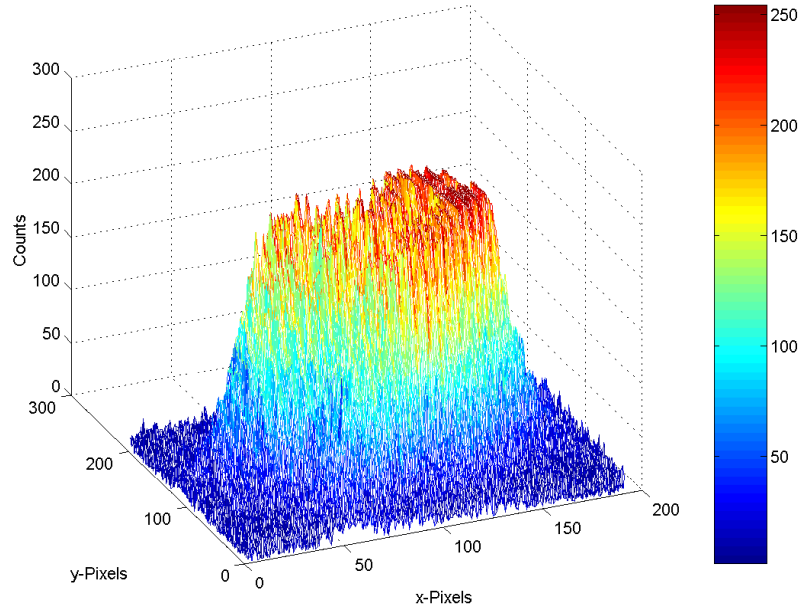


Figure 4.6: Representation in 3-D of the image from Two Direct Beam Interferometer without a polarizer filter.

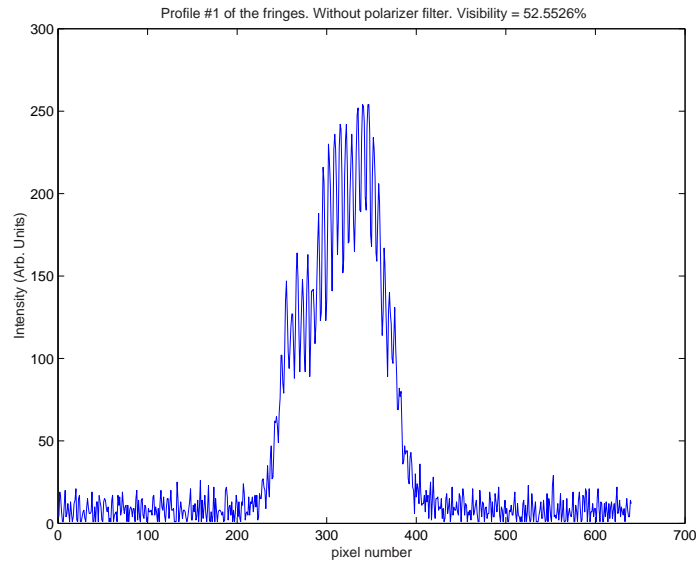


Figure 4.7: Profile of the fringes from the Direct Beam Interferometer without polarizer filter.

representation of this images in Figure 4.6 where the z-axis are the counts taken by the pixels. So, in order to obtain the visibility information from the images, the program in Matlab scanned the image looking for the profiles or sections in the x-axis direction; taking cross sections (an example of these profiles is shown in Figure 4.11) of the image. With this program it is possible to set the number of horizontal profiles wanted, and to select the x-range and y-range to scan. The number of sections depend on the x-range in the x-pixels axis. For example, in the Figure 4.4 the vertical range is from 200 to 260; so, the difference correspond to the number of sections. For the Two Direct Beam interferometer 60 sections were taken from the images with and without polarizer filters; for the Michelson Stellar Interferometer were taken 120 profiles and 140 for the Michelson Compensator. In a simple way, the visibility for each image was calculated for each of the profiles selected, and using the Michelson's criterion previously defined. A plot was obtained for each interferometer type (see Figures 4.8, 4.9 and 4.10) giving the resulting variation of visibility across each image. As the overall image profile is not flat, the scan area was chosen to ensure not selecting too wide a variation in the pedestal³.

Since the results show that for the Two Beam Interferometer without a polarizer, with a polarizer horizontally aligned and finally with a polarizer vertically aligned, the mean visibility of each set of profiles from the images was 48.47%, 79.61%

³The pedestal, vertical offset of the fringes, is dependent on the flux, and is flattest in the central region of the image

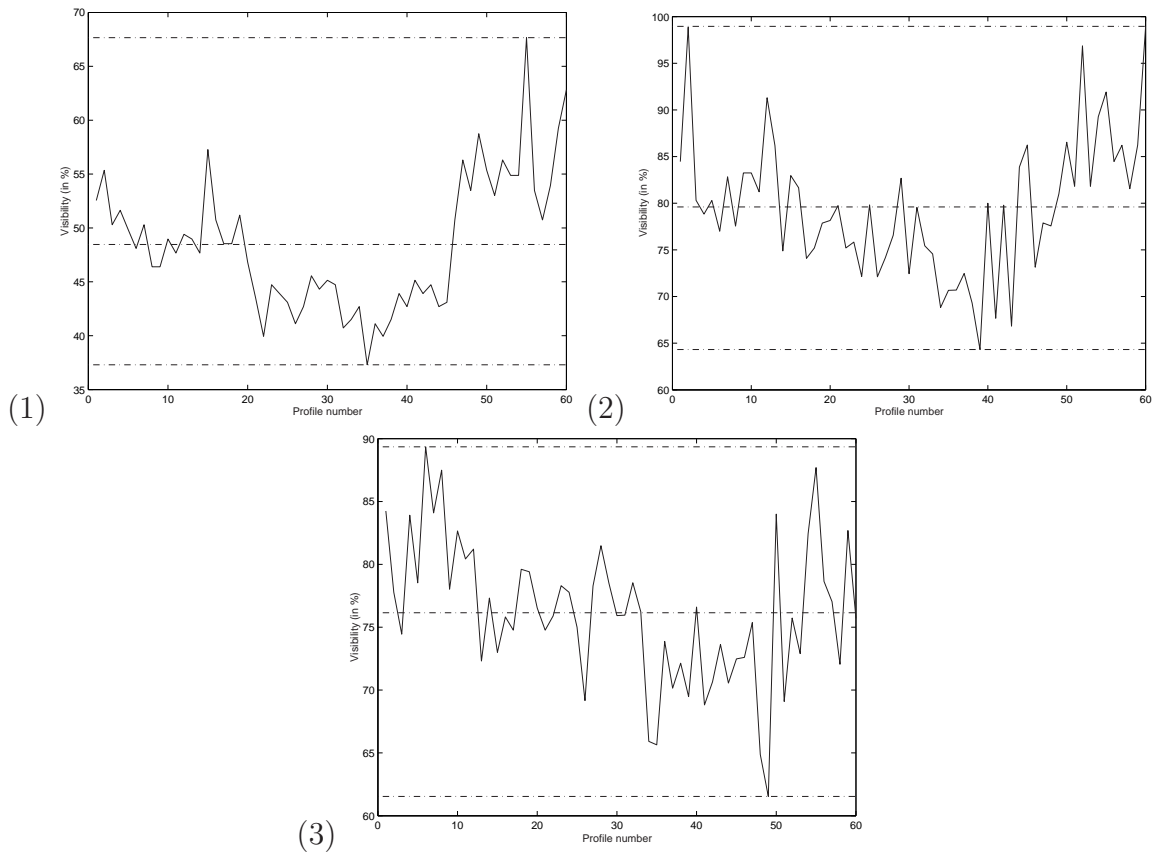


Figure 4.8: Visibility vs horizontal profile for the Two Beam Interferometer, (1) without polarizer filter, (2) with polarizer filter horizontally aligned, (3) with polarizer filter vertically aligned. The horizontal lines dashed indicate the corresponding maximum, mean and minimum values of visibility.

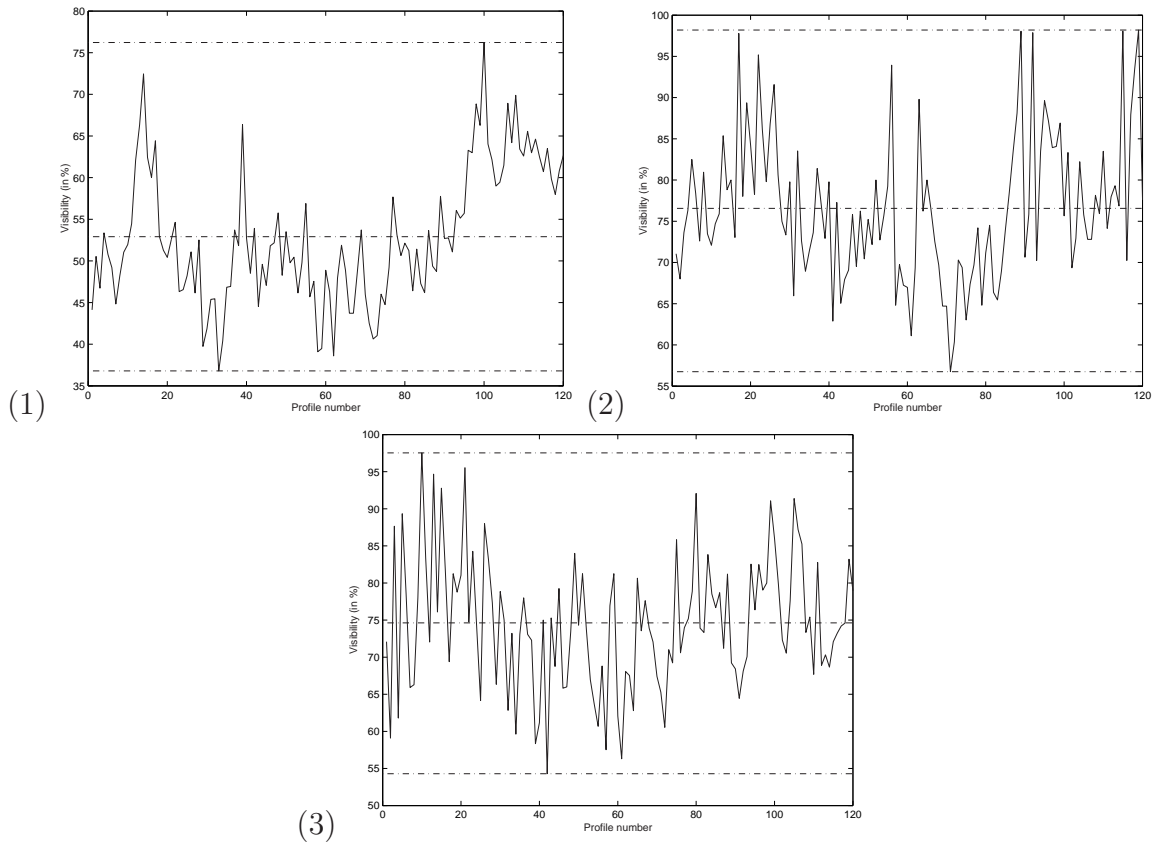


Figure 4.9: Visibility vs horizontal profile for Michelson Stellar Interferometer, (1)without polarizer filter, (2)with polarizer filter horizontally aligned, (3)with polarizer filter vertically aligned. The horizontal lines dashed indicate the corresponding maximum, mean and minimum values of visibility.

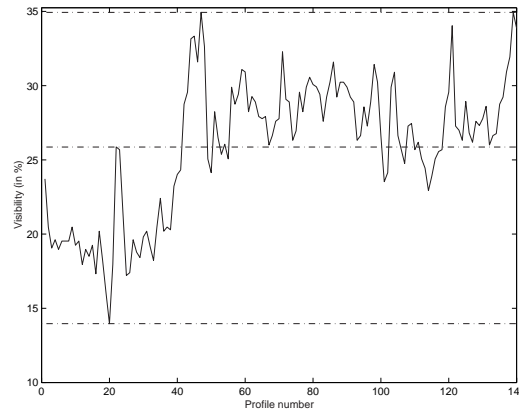


Figure 4.10: Visibility vs horizontal profile for Michelson Compensator. Without polarizer filter. The horizontal lines dashed indicate the corresponding maximum, mean and minimum values of visibility.

and 76.15% respectively. From the Michelson Stellar Interferometer for the same arrangements in the same order were 52.91%, 76.56% and 74.62%. In the case for the Michelson Compensator, the visibility calculated by this way is dramatically low at 25.86%.

4.1 New Analysis for the Fringes

Considering one of these profiles as an example (see Figure 4.11), there is no symmetry in the pattern. However, there is a curvature in the fringe pattern. Moreover the visibility measure calculated is relative to the region taken, so we can conclude that the previous measures do not represent an absolute measure of the visibility. Also, since there is a lack of homogeneity in the fringe signal, one cannot truly interpret I_{min} as the minimum fringe intensity. Also there is a large noise sig-

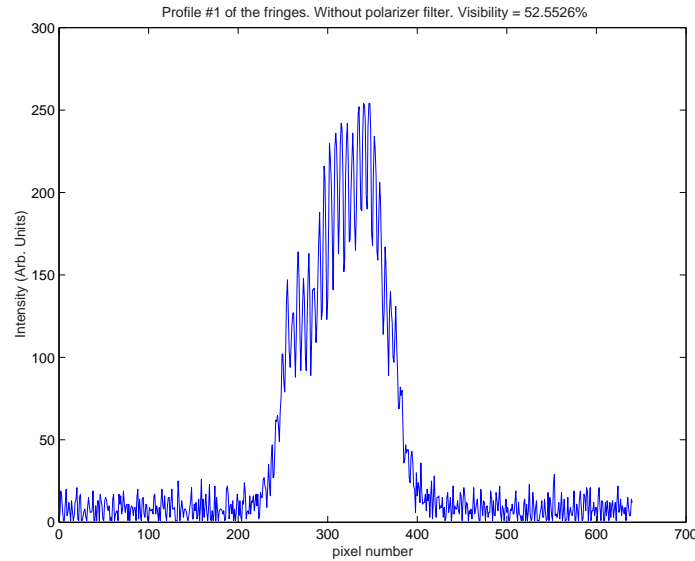


Figure 4.11: Profile of the fringes from the Direct Beam Interferometer without polarizer filter.

nal unwanted. This situation forces to establish a stronger comparison method for the visibility between the images. It is important to understand that the previous analysis in raw mode gives the visibility measures relative to a region in the complete profile. So, we can call this a regional visibility. Starting with these conditions, the calculation to obtain the visibility measures was done in two ways.

4.1.1 Method A

One way to get the visibility information is to take a profile or section of an image, that means to take the central profile, and calculate the visibility for each fringe using the Michelson's equation $V = \frac{I_{max} - I_{min}}{I_{max} + I_{min}}$; understanding as a fringe the difference between a peak and a valley in the region where the pedestal begins. After

that, an average of visibility for the total group of fringes and their error (standard deviation) was calculated. The results are shown in the Figure 4.12. In general, the visibility with the Two Beam Interferometer is high compared with the visibility from the Michelson Stellar. Another interesting detail is that comparing the visibility between the images obtained from the same interferometer, the higher measures of visibility were obtained with the polarizer filters.

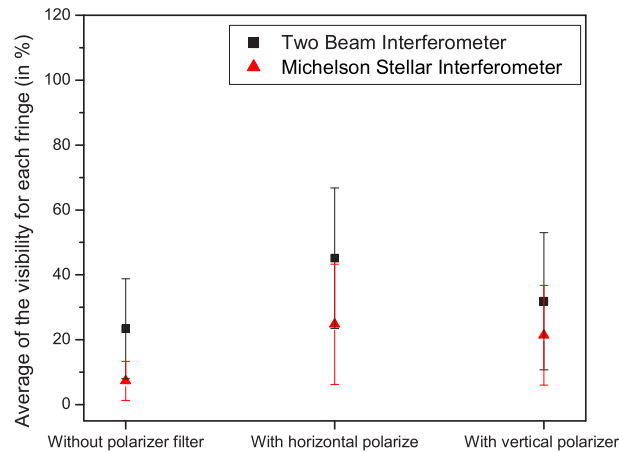


Figure 4.12: Average visibility for the images from the Two Beam Interferometer and the Michelson Stellar Interferometer with and without polarizer filters.

4.1.2 Method B

Another way to extract the visibility from the images is schematically shown in Figure 4.13. The first step is to select the central profile again and take out the pedestal signal. A strategy to take out the pedestal is to bring the complete profile

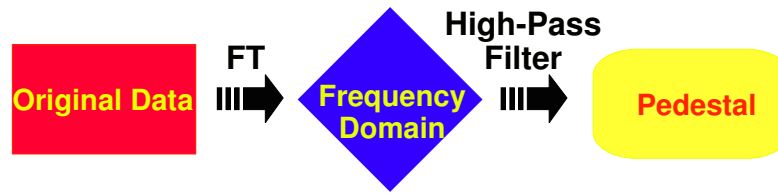


Figure 4.13: Schematic of the analysis method B.

to the spatial frequency domain using a Fourier Transform, and then with the help of a high-pass filter designed, eliminate the high spatial frequencies that are generally associated with the noise. After that, return to the space domain and to obtain a smooth function that represents the pedestal signal. This function will be subtracted from the original data and we will obtain a function as in Figure 4.14. Then, we can measure the difference in height for each fringe as in the previous method, and calculate an average of the heights and their corresponding error. However, it is necessary to normalize the pedestal function from the images of the same interferometer to guarantee that we can establish comparisons among them. To do this, I take any pedestal function as the norm and to divide each pedestal function with the norm. The average of the variation range from the maximum to the minimum of this new function is the mean scaling factor between the pedestal signals. We can now scale the average fringe heights found from each image to produce Figure 4.15. Note, we do not see symmetry in the fringe pattern.

As can be seen, the tendency is the same as in Figure 4.12; the visibility

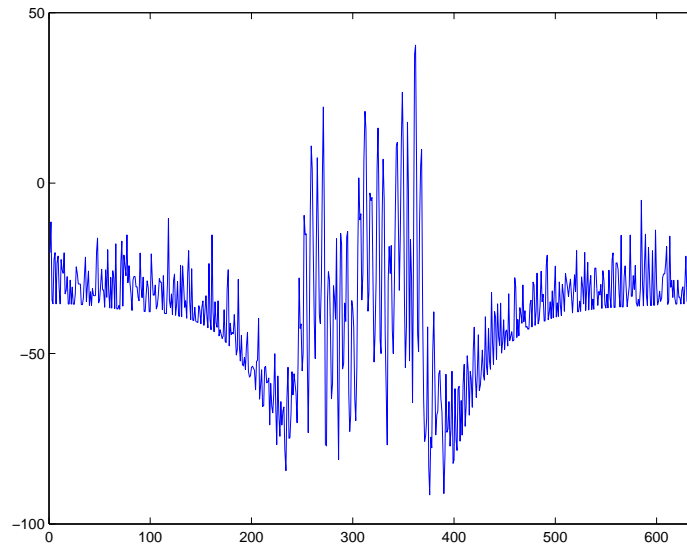


Figure 4.14: Fringes after having extracted the pedestal signal.

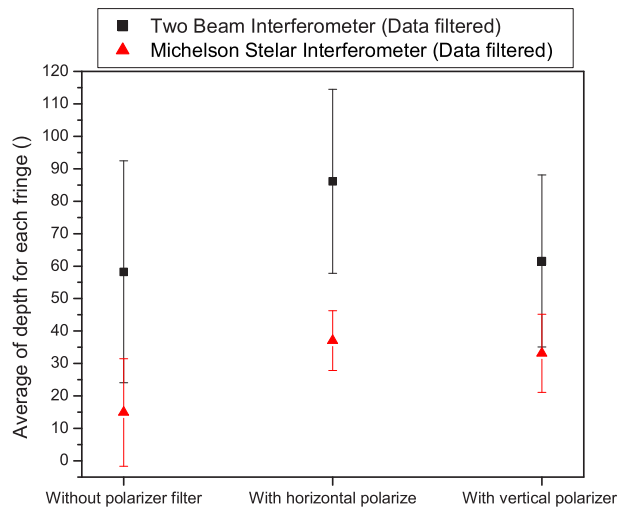


Figure 4.15: Average heights for the images from the Two Beam Interferometer and the Michelson Stellar Interferometer with and without polarizer filters.

is higher in the Two Direct Beam Interferometer than the Michelson Stellar Interferometer. Among the possible reasons are that in the Michelson Stellar Interferometer there are four more mirrors. These additional mirrors introduce losses, due to the absorption in each mirror, in the final intensity obtained at the combining system; reducing the visibility of the fringes. If we consider the four mirrors as bare aluminum, this material can reflect a 83% of the incident light in the visible range; so, the intensity of the image is reduced for each reflection by a factor of 0.83. Another possible reason is poor alignment in the beam transfer system.

Also we can see that the visibility using the polarizers is higher than without the polarizers. This is because the fringe patterns are formed only by the contributions of each arm that oscillate in the same plane as the polarizer axis; although the original intensity is also reduced, the noise is also reduced, obtaining an increment in the visibility. It is very probable that there is a preference in polarization in the arms of the interferometer. This fact indicates that there is a phase shift between the polarization states when the light is reflected, affecting the visibility of the fringes pattern (considering that the incident angle for our setups are in the range of 45° with an error neglected, the polarization effects should be important).

Viewing the case of the Michelson Compensator (which is the Michelson Stellar Interferometer with an ODL), the visibility was seen to decrease dramatically

(Figure 4.10). The mean visibility across of the image was 25.86%. Our hypothesis, based from the previous analysis that each mirror introduce a phase shift in the polarization states of the light added to a reduction of the final intensity at the combining system, indicates that the changes in polarization due to the additional reflections are the most important cause for the greater loss in the fringe signal; although we made a compensation in the optical path due to the geometrical delay. Of course, if we have added four mirrors (the ODL) the phase shift in the polarization states is increased.

The polarization effects in stellar interferometers has been treated by many investigators[3],[24],[25]. The continuous reflections in an interferometric array, are the source of phase shifts between the s and p states of polarization, resulting in a decrease of the visibility of the fringes. In order to confirm the hypothesis, a measures of the phase shift per reflection was carried out, where was prepared a optical setup as in the Figure 4.16.

While the polarizer 1 was vertical and horizontally aligned with the optical table, a phase shift was not seen when the angle θ was varied between 10° to 60° . When the polarizer 1 was set at 45° respect with the normal at the optical table, a phase shift was measured for values of $40^\circ \leq \theta \leq 60^\circ$. For example if the polarizer 1 was at 45° the minimum intensity should be seen at 135° in the polarizer 2, but at

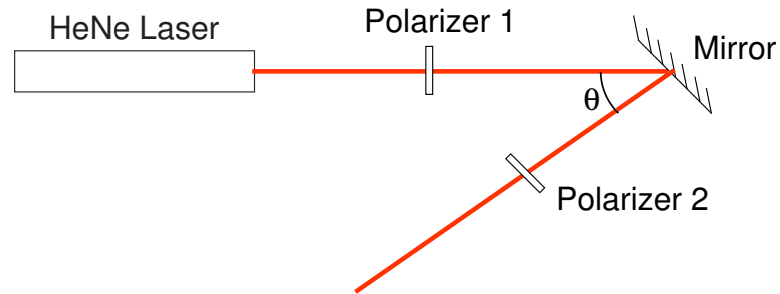


Figure 4.16: Setup for the measurements of the phase shift of the reflections.

$\theta = 45^\circ$ the minimum was seen an angle of 133° . The difference represents the phase shift. For $\theta = 50^\circ$ the phase shift found was 5° and increasing as θ increasing.

In general, it is possible to study our arrangement (see Figure 4.17) with the help of the interesting example in a report by the CHARA group[24]. In the figure we see the path of light through of two arms of the interferometer. The ovals represent mirrors. The two polarization states are represented by a square and a line segment. In the case of left arm, the s-polarization relative to the first mirror is the line segment, this initial y-axis polarization suffers a delay of $-\delta$ relative to the z-axis polarization. For each reflection the beam acquires a delay, resulting in a total phase of -3δ . On the right arm, the s-polarization is the same line. Here, the total phase is $-\delta$. So, for this state of polarization, the differences between phase shifts is -3δ .

Thus we may estimate the losses in the final intensity obtained, due to the reflections. As mentioned each aluminium mirror is assumed to be capable of

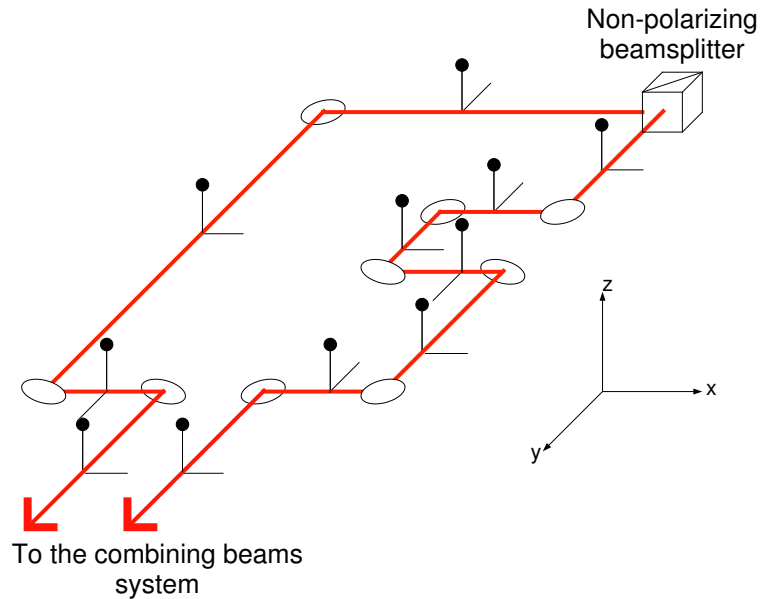


Figure 4.17: Relative phase shift between two orthogonal polarization states due reflections.

reflecting 83% of the incident light at normal incidence. So, if we have eight mirrors for example (in the left arm, including the mirrors inside the telescope), the total intensity obtained at focal plane is a factor of 0.83^8 , meaning that in the Michelson Compensator the intensities for each arm are not equal (in the right arm the total intensity is a factor of 0.83^5 including the combining system or telescope).

Chapter 5

Conclusion

This work presents the first-steps towards the development of a three element stellar interferometer with image-plane interferometry. My conclusions are:

- The first problem came with the elaboration of the motor driver cards. The simple prototype design, achieved at low cost, proved its functionality.
- Another problem with the driver cards was that no specific mount existed for it; the options were to attach the card to the motor mount or place it near the parallel port. These choices imply an increase or reduction in the cable length from the parallel port. Considering the digital signal (which is robust to noise) from the parallel port, I decide to attach the card to the motor mounts.
- One of the advantages of using a digital signal is that the cable from the parallel port may be subjected to external interferences with little signal loss. It is possible to extend the cable to ≈ 100 meters successfully. But, eventually it would be appropriate to think of a form of shielding for the cable.

- As for the optical arrangement, there was a restriction applied to the minimum height of the setup. This is due to the position of the pulley on the motor mount. If we consider the case of the calibration mount in Figure 3.11, although it is not the mount used for the ODL, it does show the relative position between the motor and the pulley. The diameter of the pulley restricts the micrometer screw height.
- The results from the calibration measurements of the motors show that it is possible to reach precise positioning but only in one direction; the loss of precision in two directions and, extrapolating, in any oscillating mode shows that the motors will not work to compensate for atmospheric fringe drift, but only for the gross geometric delay. The motors are good for other purposes. I have thought of using them to motorize the artificial sources of light for system alignment.
- The independence of the three parallel ports of the PCs under Linux was demonstrated. But, this independence does not imply that the motors will be working independently in real-time, as in the ideal case. The speed of the processor will give us the perception of the work in real-time. I recommend testing the control loop to see if it operates in real time, otherwise one will need to have a computer for each motor.
- In general for the arrangement, reflections of greater than 45° cause severe phase shift between the orthogonal states of polarization of the light. So, it is better

to design again the optical setup for the ODL. I have outlined a design that, while probably expensive, sets the reflections of the incident beams to near normal (Figure 5.1). The disadvantage in the new design is that the numbers of reflections has increased; therefore the overall quantity of light flux that arrives to the combination system is reduced in comparison of if we use our design. So, in spite of the cost and the fact that the combining system loses light, the visibility of the fringes should improve giving us more signal.

- Since for high visibility fringes, the polarization state from each arm should be equal, this implies that the optical system will have to be symmetric in terms of the reflections.
- Another alignment method for the optical system is needed. The current one does not guarantee the parallelism between the two arms, and so this will be made more complex with three arms.
- We have seen that with a monochromatic source of light and intensity high levels, we find problems associated to the visibility of the fringes; therefore we expect more pronounced difficulties when using an artificial white light source to simulate a star.

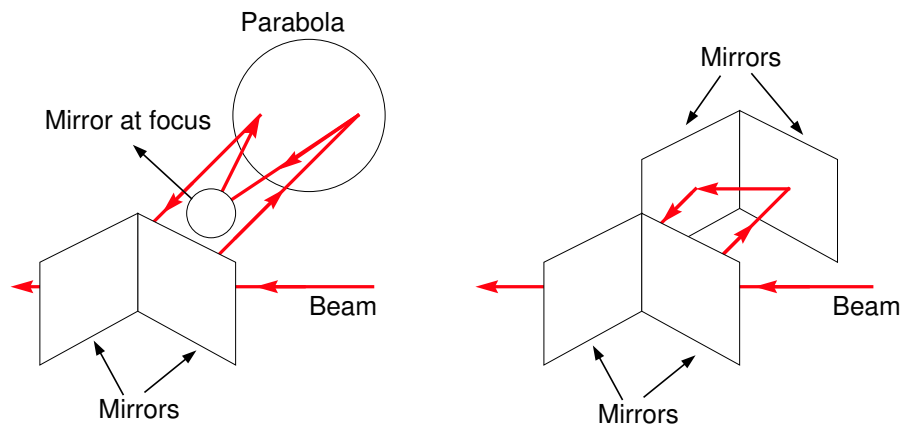


Figure 5.1: (left) The proposed design for the ODL and (right) the current design.

Appendix A

Matlab Scripts

In 1-D, the script simulating a rectangle function of unit height and base is:

```
close all; % close all figures
clear all; % clear all variables
resolution=1000; % number of points in our space
xspace=linspace(-3,3,resolution); % build x-space
yspace=xspace*0; % set to 0 y-space
for i=1:dimension
    if (xspace(1,i) <= 0.5) & (xspace(1,i) >= -0.5)
        yspace(1,i)=1; % assigns function values
    end
end
figure(1),plot(xspace,yspace),xlabel('x-axis'),ylabel('y-axis')
ft_func=fftshift(abs(fft(yspace)));
ft_func_sqrt=(ft_func).^2;
figure(2),plot(xspace,ft_func)
```

And the complete 2-D script that make a FFT over a circular function simulating a circular aperture is:

```
close all;
clear all;
dimension=input('Cual es la dimension de la matriz?')
n=120;
A=zeros(dimension);

for i=1:dimension
```

```

    for j=1:dimension
        if (i-dimension/2)^2 + (j-dimension/2)^2 <= n
            A(i,j)=1;
        end
    end
end

fouriertr=fftshift(abs(fft2(A)));

figure(2),imagesc(fouriertr),colormap(gray),axis off;

```

The 2-D script that carried out a simulations of two apertures, showing the fringes and profile is:

```

close all;
clear all;
dimension=150;
radius=5;
A=zeros(dimension);

for i=1:dimension
    for j=1:dimension
        if (i-dimension/2)^2 + (j-dimension/2)^2 <= radius^2
            A(i,j-20)=1;
        end
    end
end

for k=1:dimension
    for l=1:dimension
        if (k-dimension/2)^2 + (l-dimension/2)^2 <= radius^2
            A(k,l+20)=1 %*exp(sqrt(-1)*4); % exp(i*phi) is the fase factor
        end
    end
end

fouriertr=fftshift(abs(fft2(A)));
fouriertr= fouriertr / max(max(max(fouriertr)));

```

```
figure(1),imagesc(A),colormap(gray),axis off;  
figure(2),imagesc(fouriertr),colormap(gray),axis off;  
%figure(3),mesh(fouriertr);  
figure(4),plot(fouriertr(75,.,:))
```

Appendix B

Code in C language

```
/* motor.c - control a unipolar stepper motor
 *
 * Author : Armando Yance
 * Date   : 18 July 2001
 * Description :
 * Single coil excitation for a 5 wire
 * for a unipolar stepper motor (rescued from a floppy drive)
 * using a PC -- {\em compile code with gcc: gcc -O2 motor.c -o motor}
 * Linux code needs to run as root.
 *
 *          7   6   5   4   3   2   1   0   I/O Port
 *          +---+---+---+---+---+---+---+---+ =====
 * Data |   |   |   |   | C4| C3| C2| C1| Base = 278/378/3BC Hex
 *          +---+---+---+---+---+---+---+---+
 */

#include <stdio.h>
#include <unistd.h>
#include <asm/io.h>

#define BASEPORT0 0x3bc /* lp0 */
#define BASEPORT 0x378 /* lp1 */
#define BASEPORT2 0x278 /* lp2 */

void Delay(void)
{
    /* Sleep for a while (in us) */
    usleep(1000);
}
```

```
void KeyPress(void)
{
    printf(" <Press any key to continue>");
    while (!getchar()); /* wait for key press */
    printf("\n");
}

int main()
{
    int i;

    /* Get access to the ports */
    if (ioperm(BASEPORT, 3, 1)) {perror("ioperm"); exit(1);}

    /* Set the data signals (D0-7) of the port to all low (0) */
    outb(0x0, BASEPORT);
    fprintf(stderr, "\nAll lines set to OFF.");
    KeyPress();

    fprintf(stderr, "Clockwise rotation\n");

    for (i=1; i<=25; i++)
    {
        outb(0x08, BASEPORT); Delay();
        outb(0x0c, BASEPORT); Delay();
        outb(0x04, BASEPORT); Delay();
        outb(0x06, BASEPORT); Delay();
        outb(0x02, BASEPORT); Delay();
        outb(0x03, BASEPORT); Delay();
        outb(0x01, BASEPORT); Delay();
        outb(0x09, BASEPORT); Delay();
        fprintf(stderr, ".");
    }
    KeyPress();

    fprintf(stderr, "Anticlockwise rotation\n");

    for (i=1; i<=25; i++)
    {
        outb(0x09, BASEPORT); Delay();
        outb(0x01, BASEPORT); Delay();
```

```
        outb(0x03, BASEPORT); Delay();
        outb(0x02, BASEPORT); Delay();
        outb(0x06, BASEPORT); Delay();
        outb(0x04, BASEPORT); Delay();
        outb(0x0c, BASEPORT); Delay();
        outb(0x08, BASEPORT); Delay();
        fprintf(stderr, ".");
    }
    KeyPress();

    outb(0x0, BASEPORT);
    fprintf(stderr, "All lines set to OFF again.");
    KeyPress();

    /* We don't need the ports anymore */
    if (ioperm(BASEPORT, 3, 0)) {perror("ioperm"); exit(1);}

    exit(0);
}
```

Appendix C

Calculation for the Driver Card Circuit Values

There are two ways to do the calculation and they are:

C.1 Case 1

This is the worst case, where $I_c|_{\text{total}}$ is maximized. All resistances are connected to ground – closed circuits.

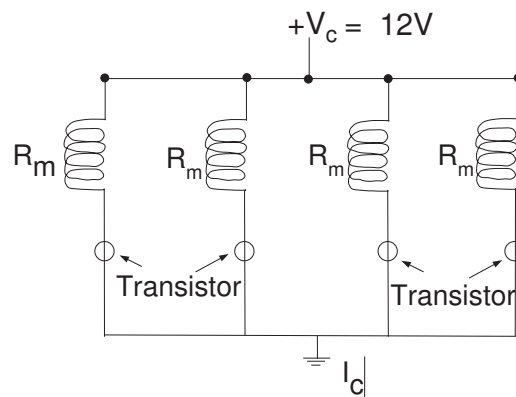


Figure C.1: Figure shown the circuit with all resistances connected to ground.

$$R|_{\text{equiv}} = \left(\frac{1}{R_m} \times 4 \right)^{-1} = \frac{75}{4} \sim 18.75\Omega \quad (\text{C.1})$$

$$\therefore I_c = \frac{V_c}{R_{m|_{\text{equiv}}}} = \frac{12}{18.7} = 640\text{mA} \quad (\text{C.2})$$

C.2 Case 2

The transistor action, as well known, is:

$$I_c = \gamma I_b \quad (\text{C.3})$$

Where I_c is the current flowing through the collector, and I_b is the current flowing into the base transistor.

We know that the I_c required to energise the motor coil (R_m) is

$$I_c = \frac{V_c}{R_m} = \frac{12V}{75\Omega} = 160\text{mA} \quad (\text{C.4})$$

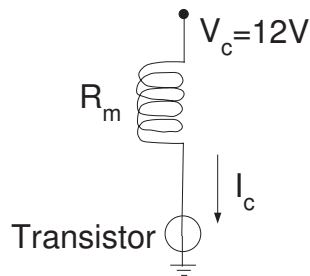


Figure C.2: Figure showing the current flowing through of a circuit branch.

The transistor 2N2222 has a typical gain (at low frequency) of $\gamma \sim 10$. Therefore we require an I_b of 16mA.

We know that the design voltage of a parallel port is ideally 5V, although in reality this may vary between 3V and 5V depending on the parallel port circuit design. So to convert this voltage to the appropriate I_b , we must use a resistor R_b of value:

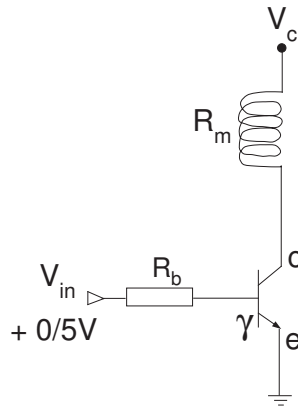


Figure C.3: Sketch used to calculate R_b .

$$\frac{5}{R_b} \times 10 = 160\text{mA} \Rightarrow R_b = 312\Omega \quad (\text{C.5})$$

But the nearest standard value is 330 Ω .

$$\therefore I_c = \gamma \times I_b = \frac{5}{330} \times 10 = 151\text{mA} \quad (\text{C.6})$$

Appendix D

Images and Graphs of Data

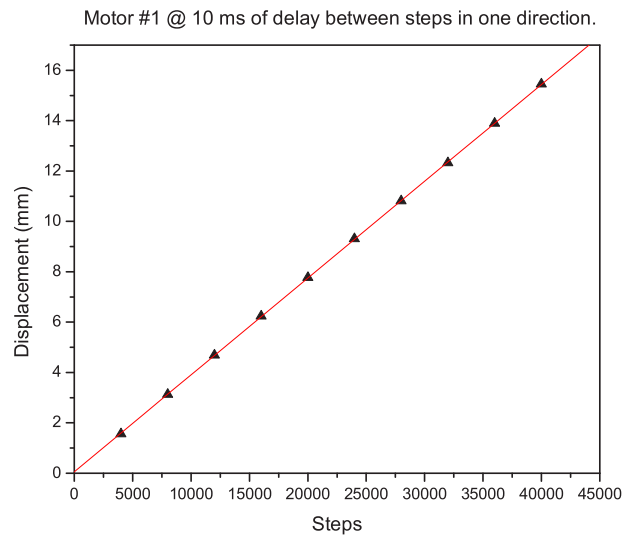


Figure D.1: Calibration data of the stepper motors #1 @ 10ms of delay in one direction.

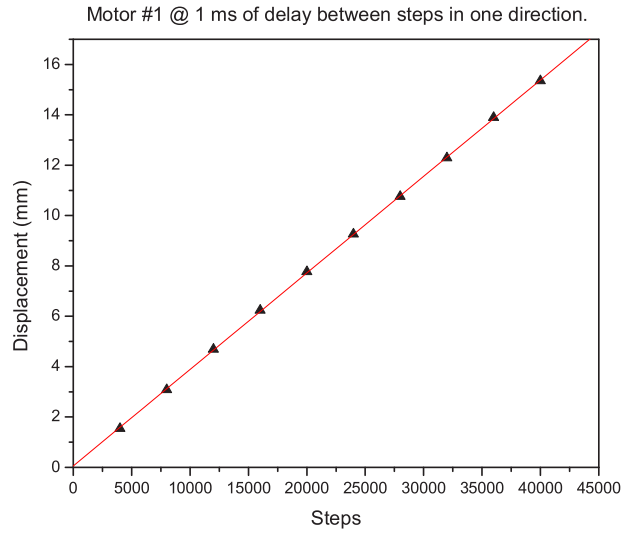


Figure D.2: Calibration data of the stepper motors #1 @ 1ms of delay in one direction.

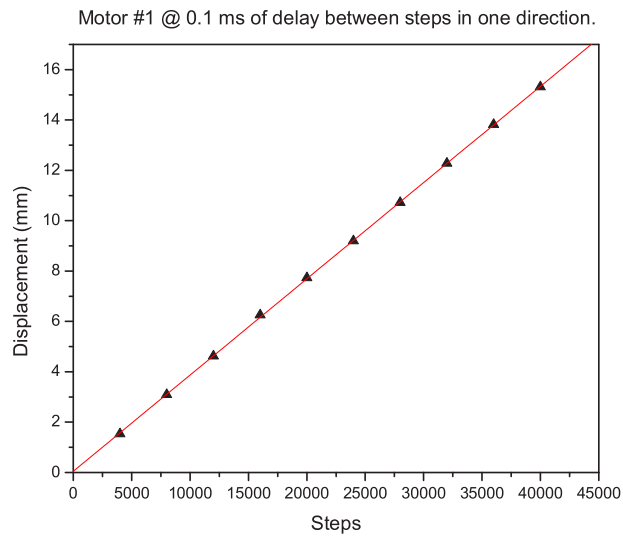


Figure D.3: Calibration data of the stepper motors #1 @ 0.1ms of delay in one direction.

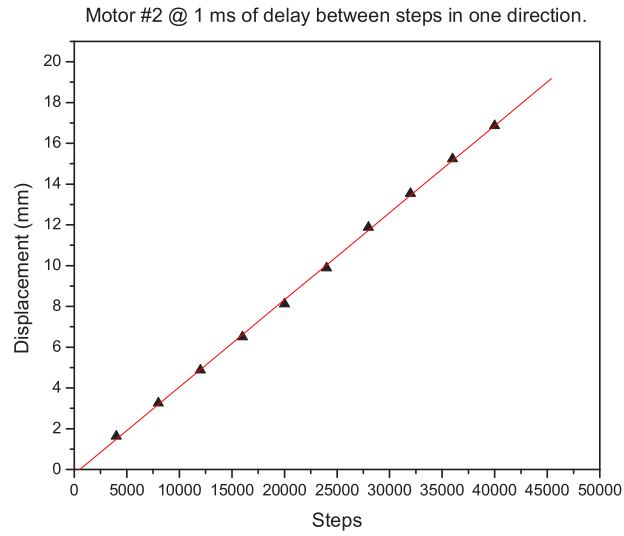


Figure D.4: Calibration data of the stepper motors #2 @ 1ms of delay in one direction.

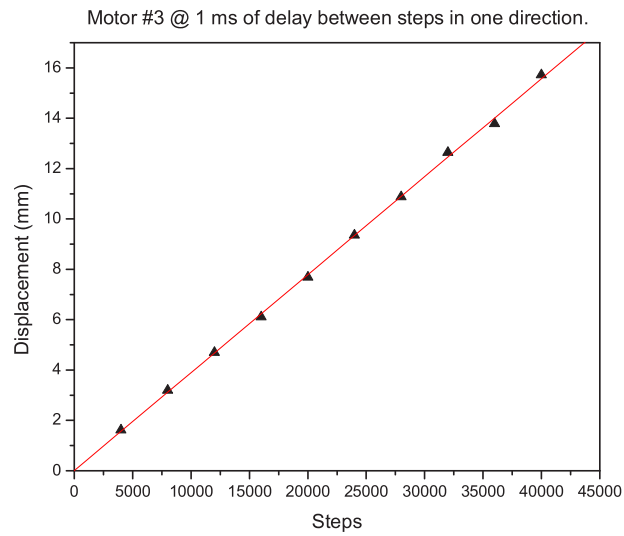
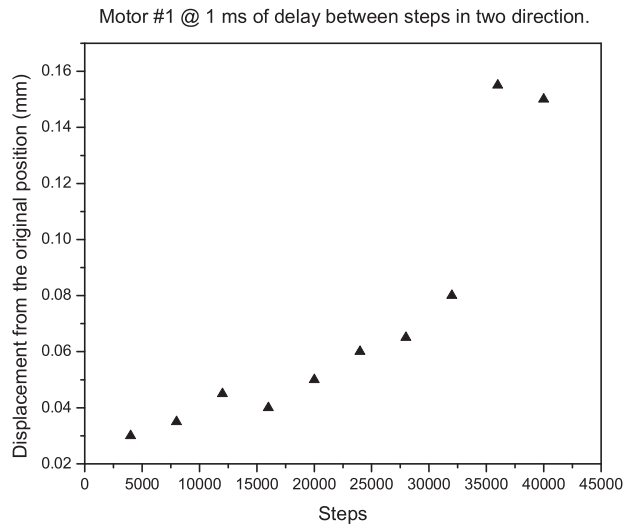


Figure D.5: Calibration data of the stepper motors #3 @ 1ms of delay in one direction.



(1)

Figure D.6: Calibration data of the stepper motor #1 @ 1 ms in two directions.

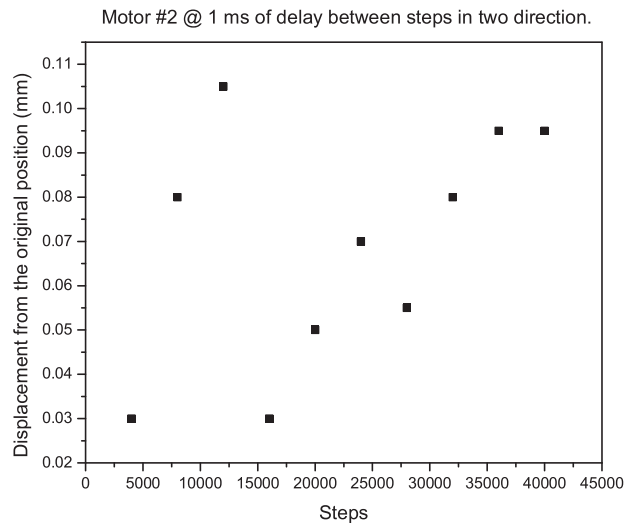


Figure D.7: Calibration data of the stepper motor #2 @ 1 ms in two directions.

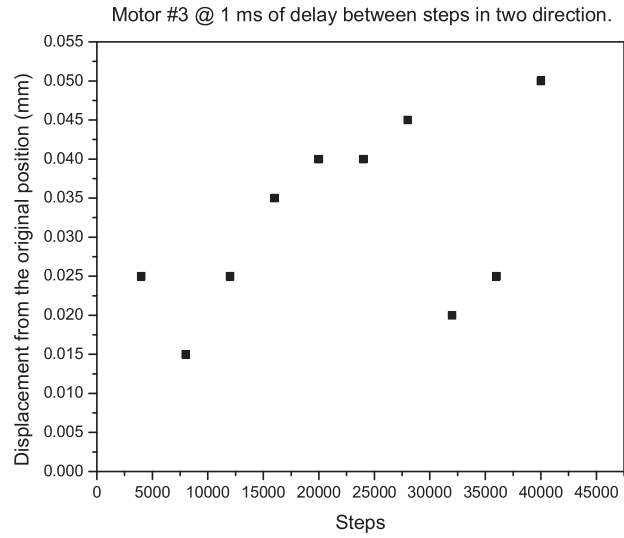


Figure D.8: Calibration data of the stepper motor #3 @ 1 ms in two directions.

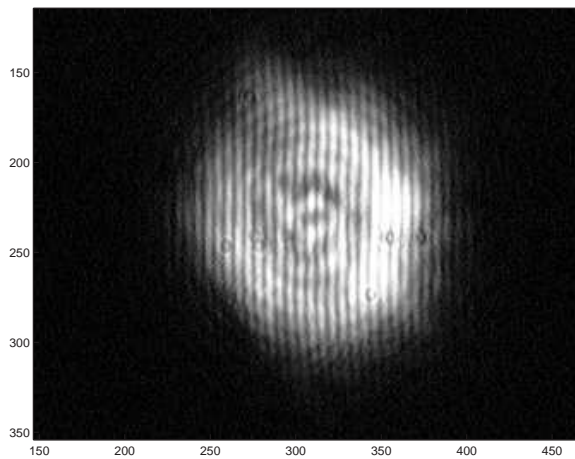


Figure D.9: First fringes obtained from Direct Two beam Interferometer without polarizer.

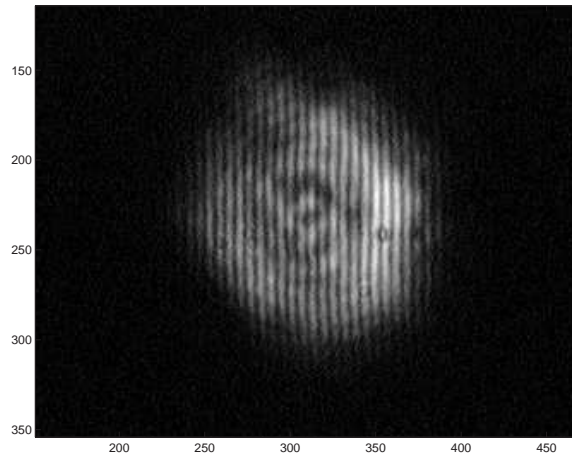


Figure D.10: Fringes from Direct Two beam Interferometer with horizontal polarization filter.

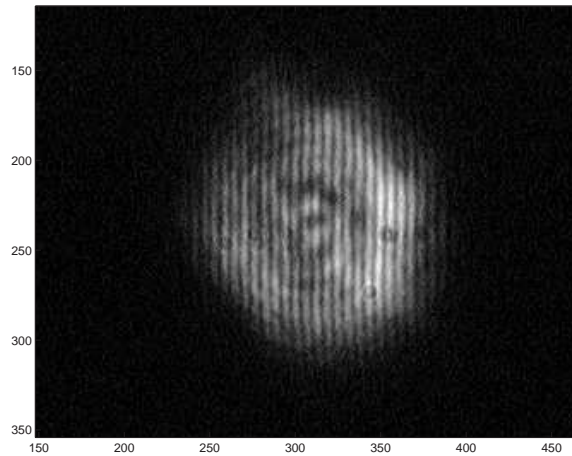


Figure D.11: Fringes from Direct Two beam Interferometer with vertical polarization filter.

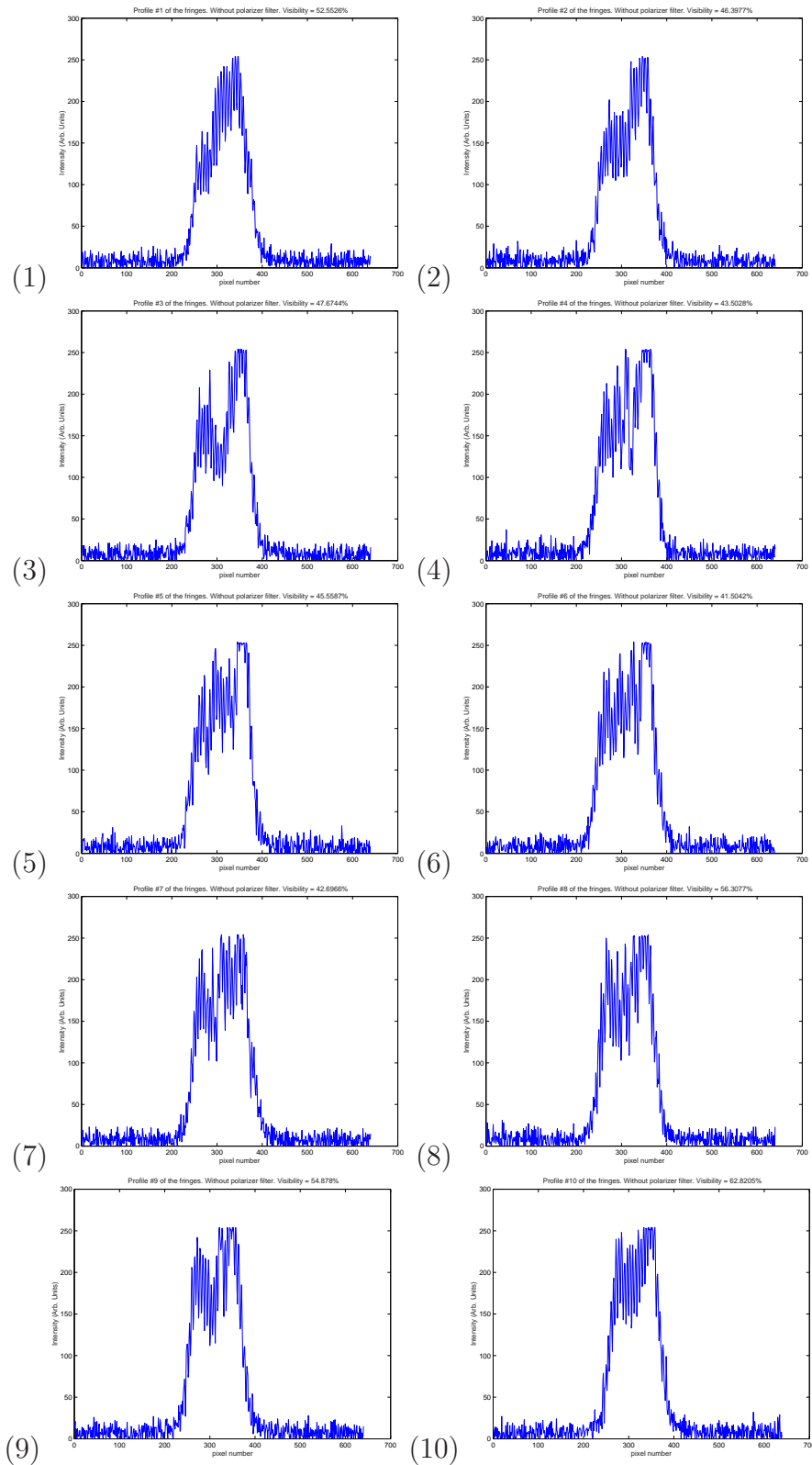


Figure D.12: Graphs of intensity vs pixels for each profile from Direct Two Beam Interferometer without polarizer for 10 horizontal lines selected for the single image.

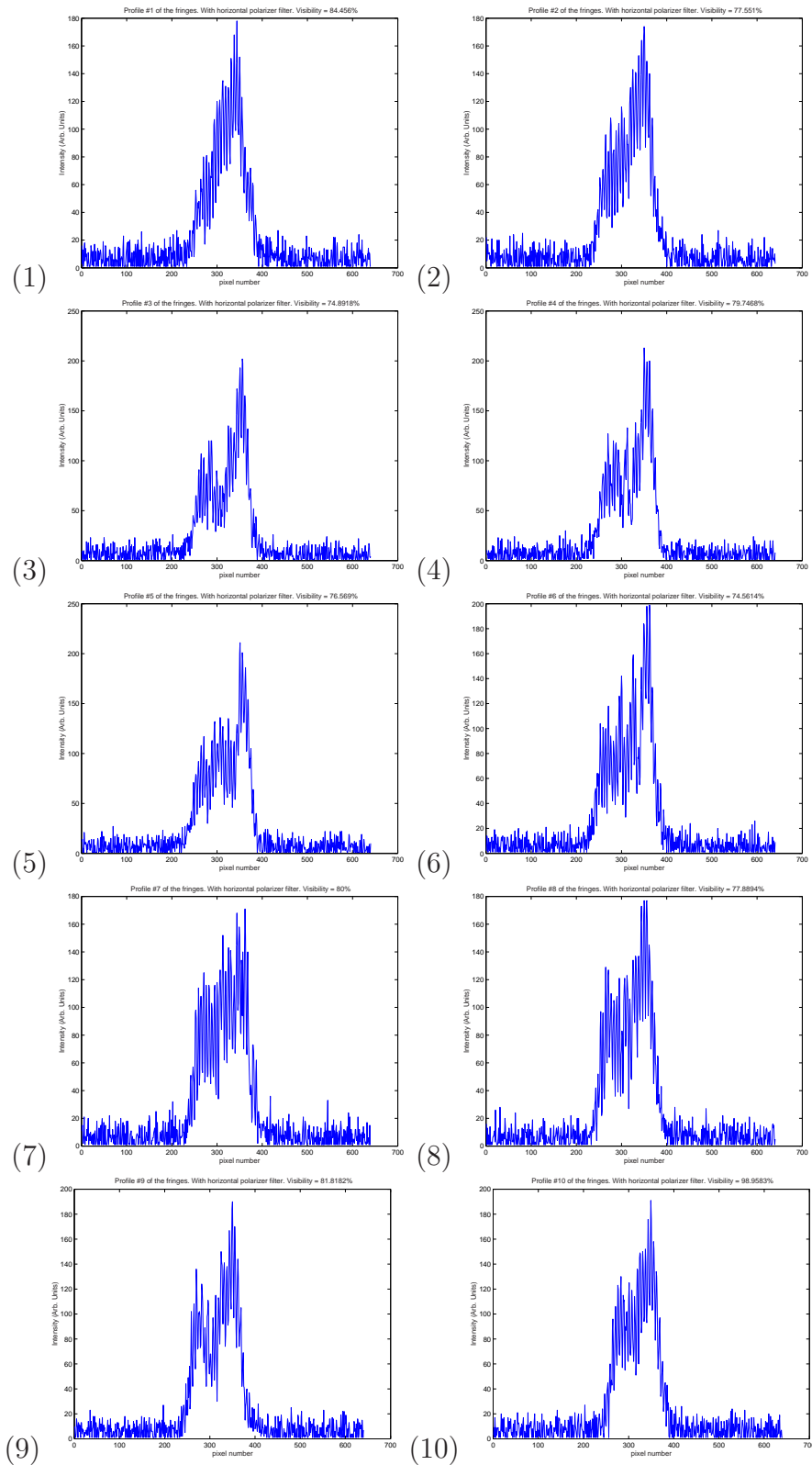


Figure D.13: Graphs of intensity vs pixels for each profile from Direct Two Beam Interferometer with horizontal polarization for 10 horizontal lines selected for the single image.

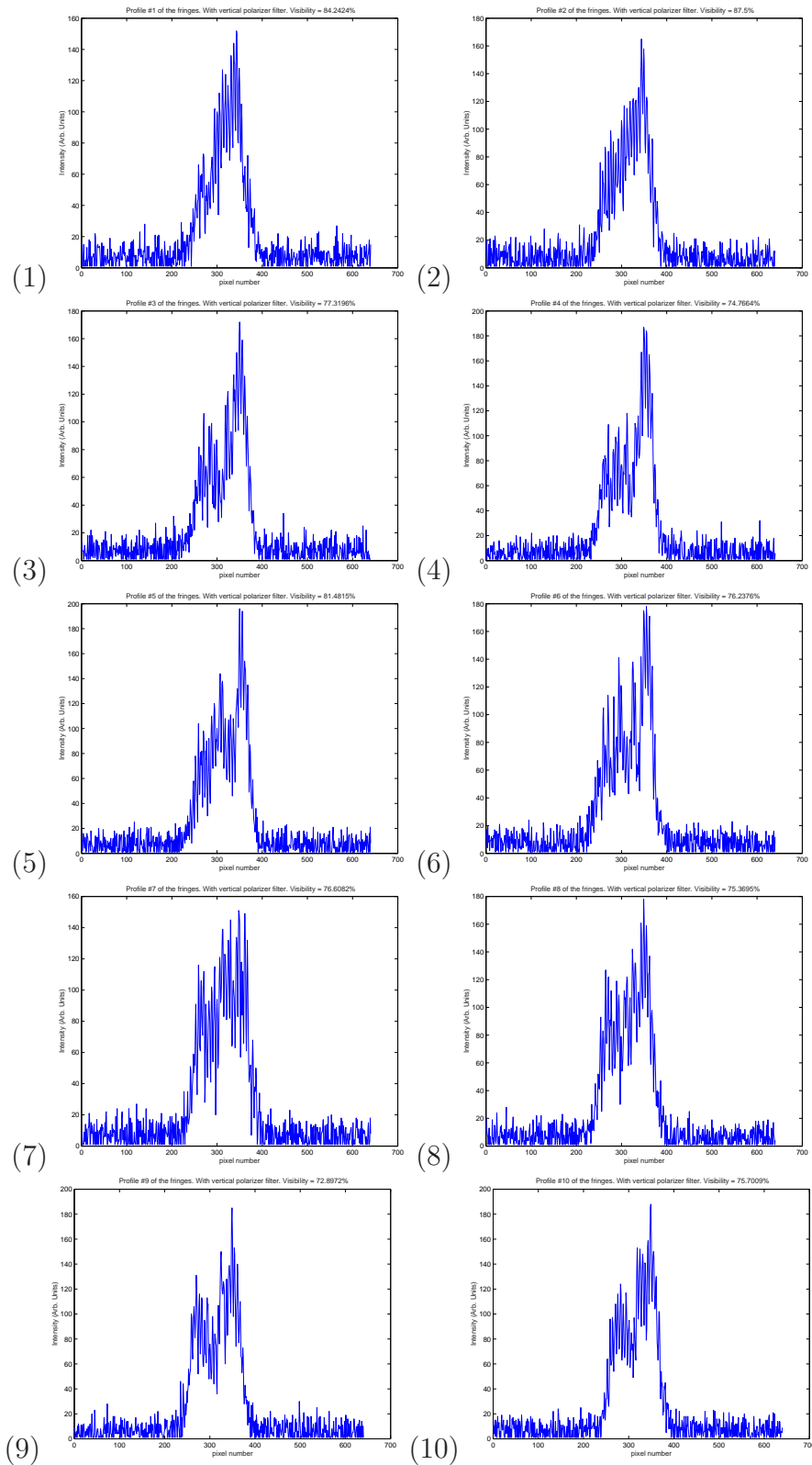


Figure D.14: Graphs of intensity vs pixels for each profile from Direct Two Beam Interferometer with vertical polarization for 10 horizontal lines selected for the single image.

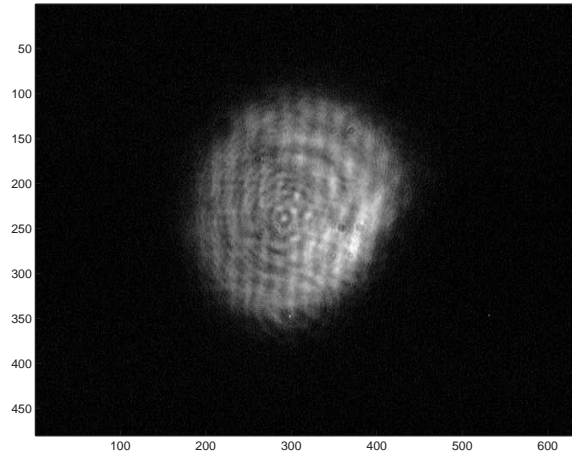


Figure D.15: Fringes obtained from Michelson Stellar Interferometer without polarization filter.

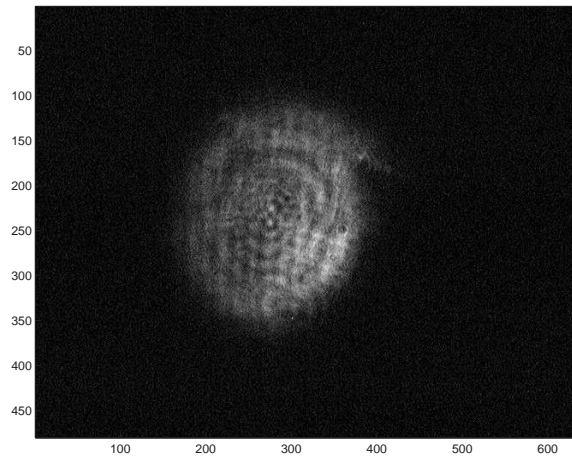


Figure D.16: Fringes obtained from Michelson Stellar Interferometer with horizontal polarizer.

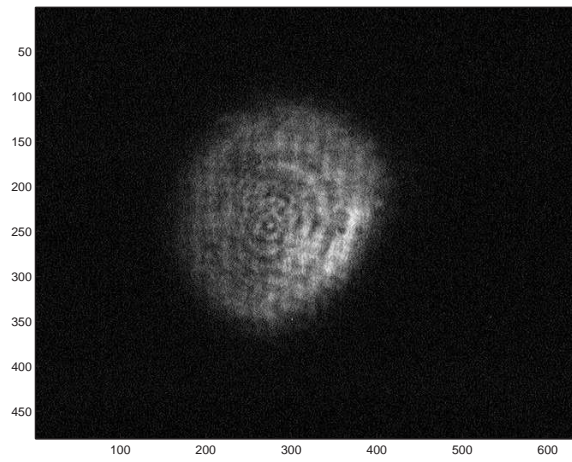


Figure D.17: Fringes obtained from Michelson Stellar Interferometer with vertical polarizer filter.

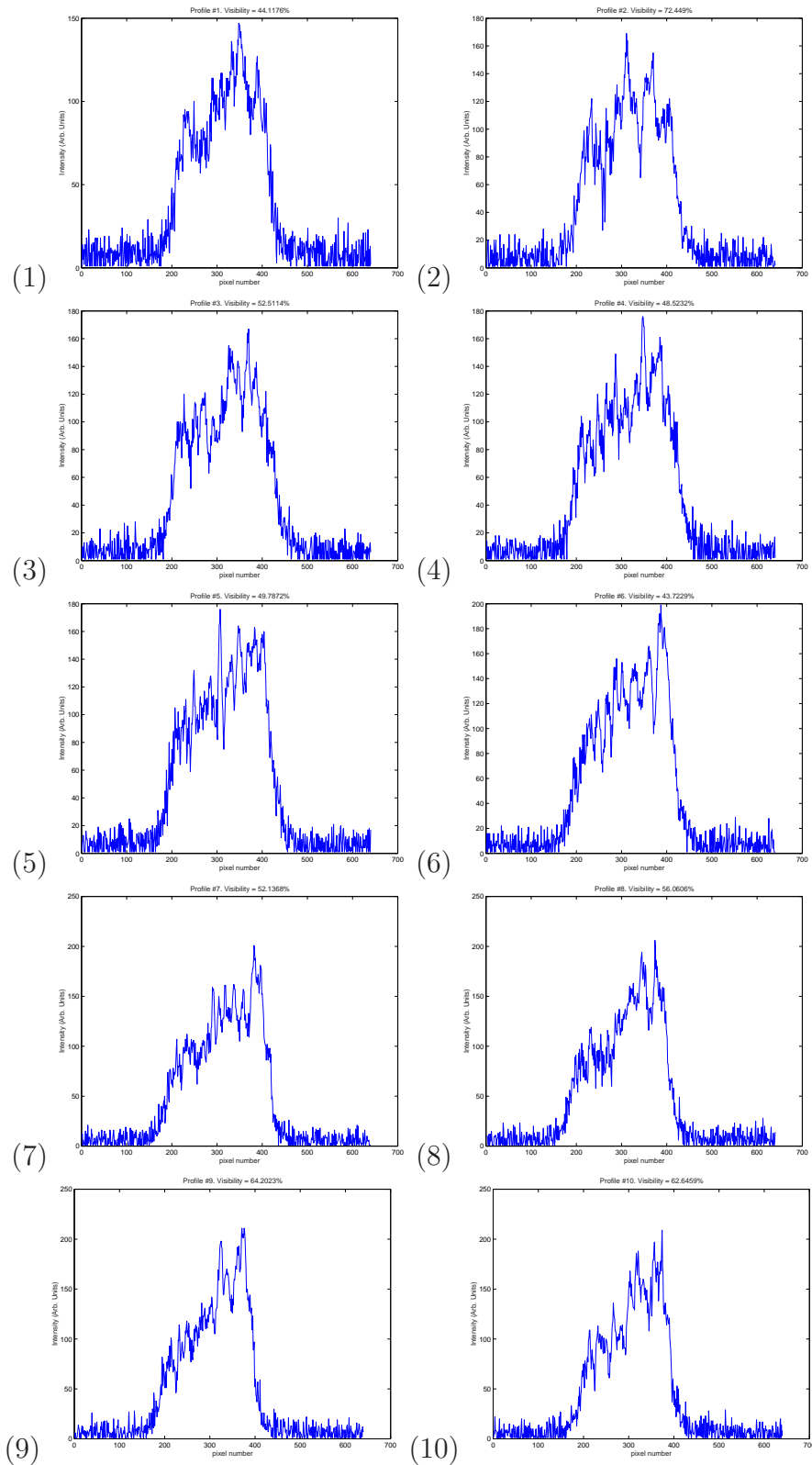


Figure D.18: Graphs of intensity vs pixels for each profile from Michelson Stellar Interferometer without polarization filter for 10 horizontal lines selected for the single image.

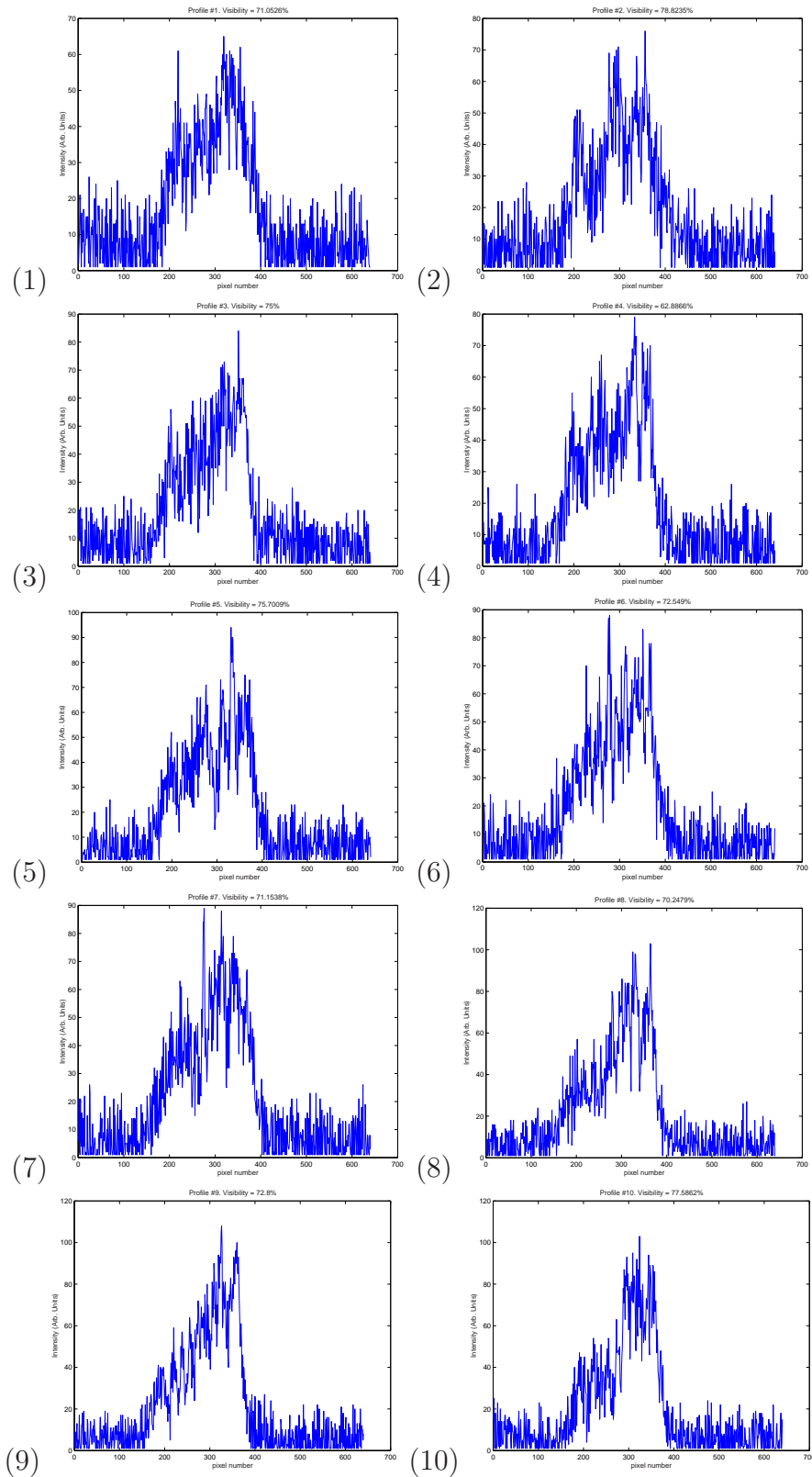


Figure D.19: Graphs of intensity vs pixels for each profile from Michelson Stellar Interferometer with horizontal polarization filter for 10 horizontal lines selected for the single image.

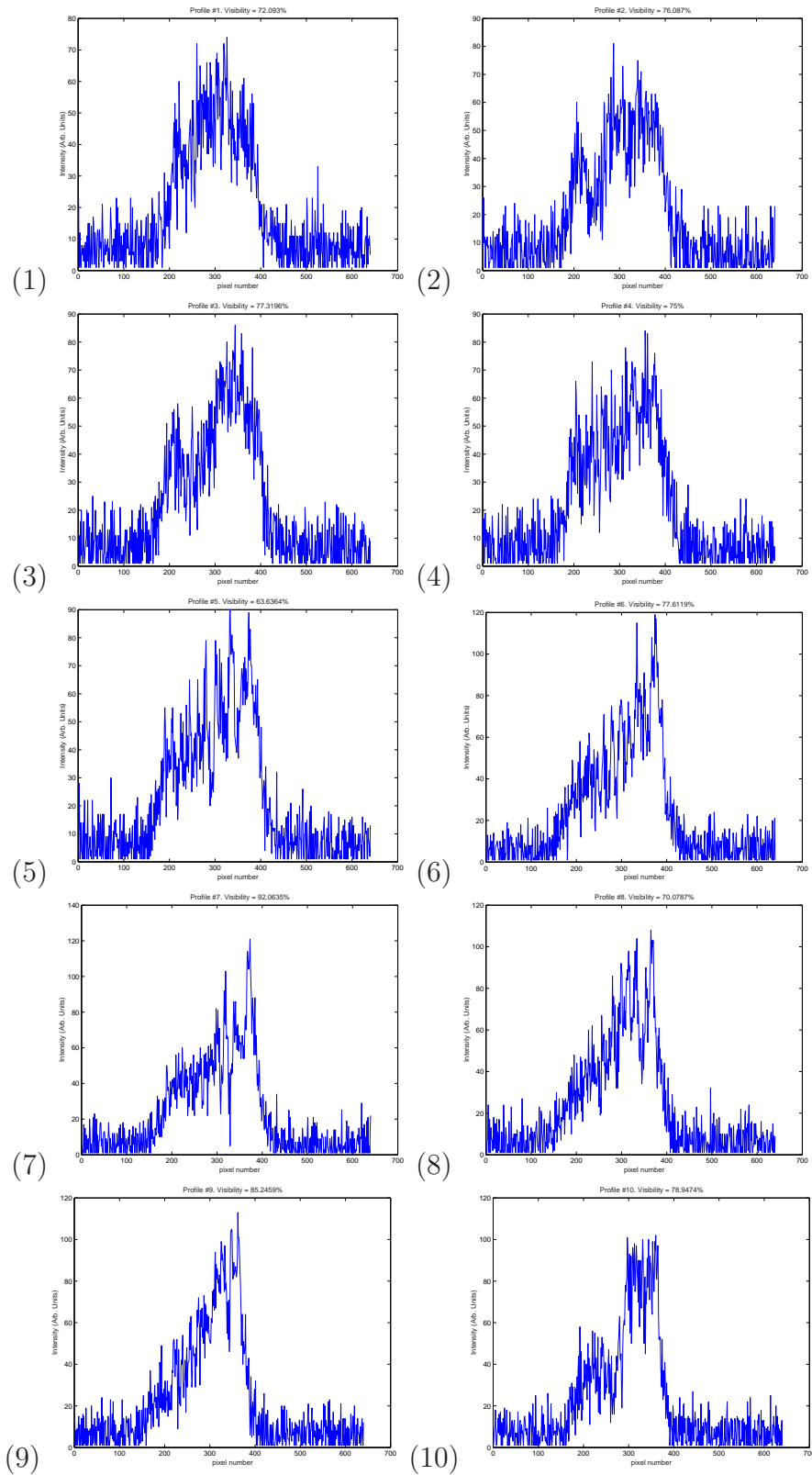


Figure D.20: Graphs of intensity vs pixels for each profile from Michelson Stellar Interferometer with vertical polarization filter for 10 horizontal lines selected for the single image.

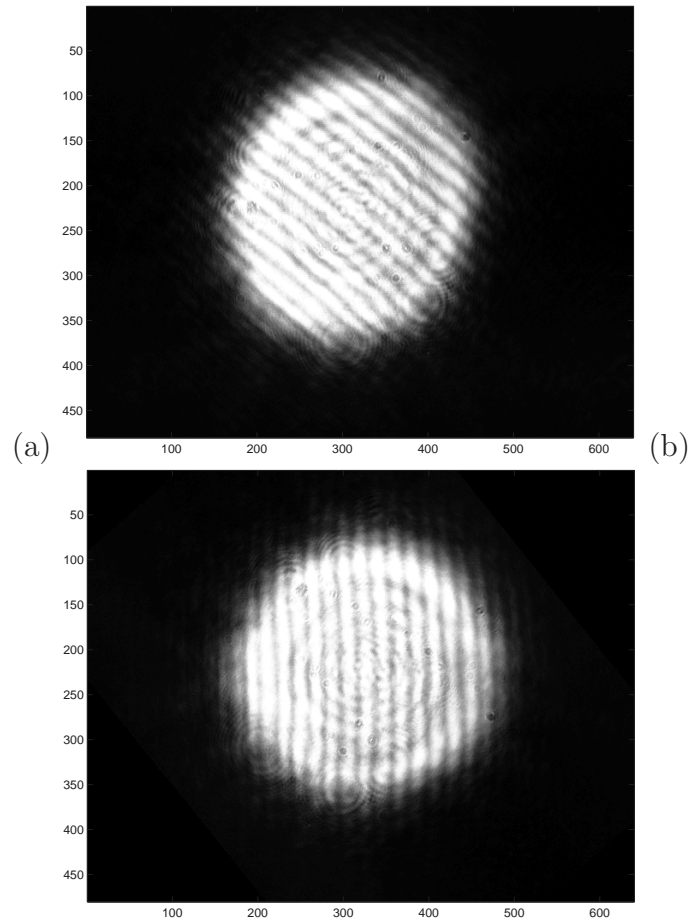


Figure D.21: Fringes obtained from Michelson Stellar Interferometer with ODL. (a) Original image, (b) Image rotated.

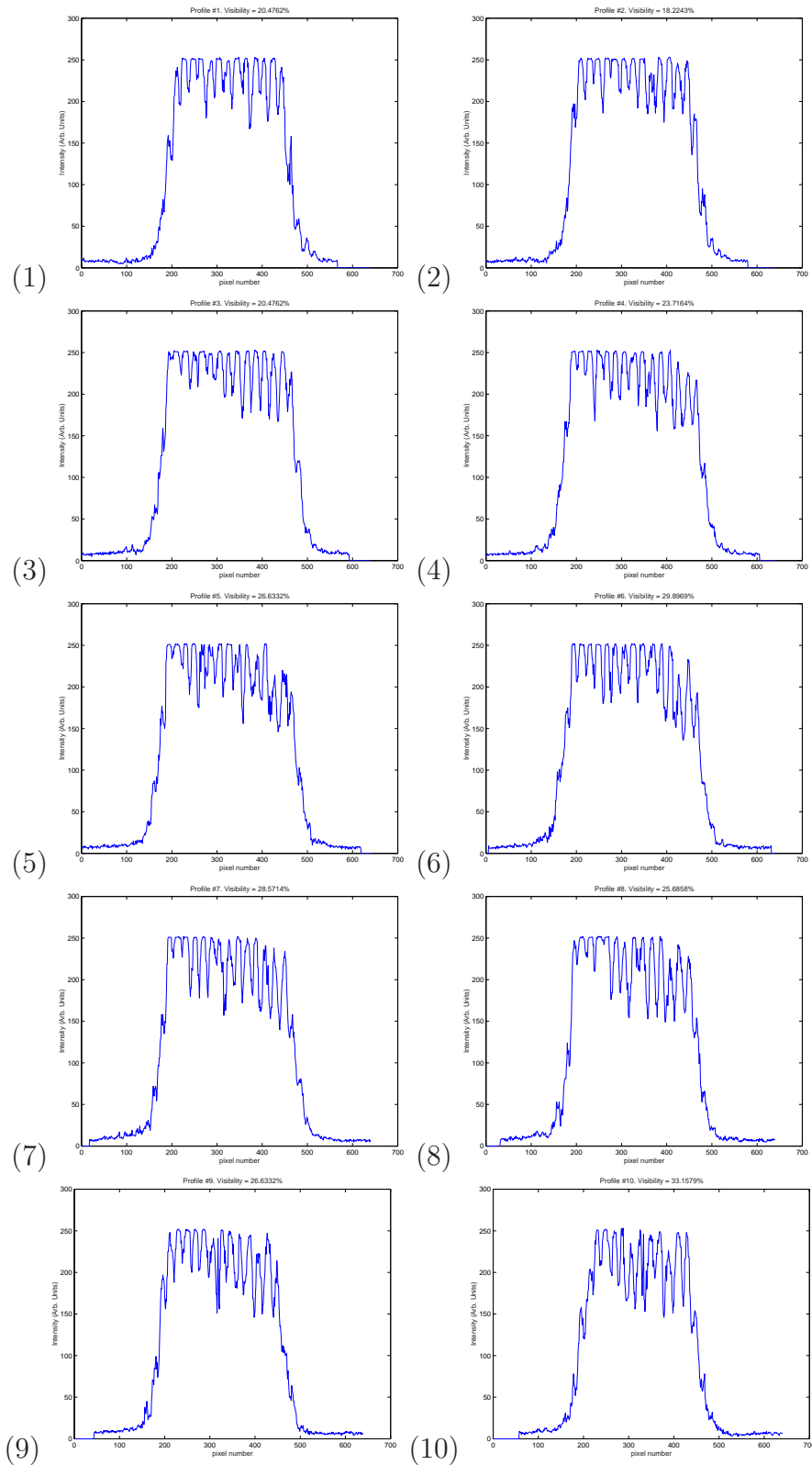


Figure D.22: Graphs of intensity vs pixels for each profile from Michelson Stellar Interferometer with ODL for 10 horizontal lines selected for the single image.

Bibliography

- [1] A. Labeyrie, *Astron. Astrophys.* **6**, 85 (1970).
- [2] Gendron E., Léna P., *Astron. Astrophys. Suppl. Ser.*, **111**, 153 (1995).
- [3] W. Traub, “polarization effects in stellar interferometers” in *High Resolution Imaging by Interferometry*, F. Merkle, ed., ESO Conf. Proc. 29 (1988).
- [4] M. P. J. L. Chang, *DAFI: A Single Mode Optical Fibre Interferometer for Astronomy*, Ph. D. Thesis, University of Durham, (1998).
- [5] A. H. L. Fizeau, *C. R. Acad. Sci.*, **66**, 932 (1868).
- [6] E. Stephan, *C. R. Acad. Sci.* **78**, 1008 (1874).
- [7] A. A. Michelson, *Nature* **45**, 160 (1891).
- [8] A. A. Michelson, F. G. Pease, *Astrophys. J.* **53**, 249 (1921).
- [9] F. G. Pease, *Sci. Am* **143**, 290 (1930).
- [10] F. G. Pease, *Ergeb. Exakten Naturwiss* **10**, 84 (1931).

- [11] R. Hanbury Brown, J. Davis, L. R. Allen, *Mon. Not. R. Astron. Soc.* **137**, 375 (1967).
- [12] R. H. Brown, J. Davis, L. R. Allen, *Mon. Not. R. Astron. Soc.* **167**, 121 (1974).
- [13] A. Labeyrie, *Astrophys. J.*, **196**, L71, (1975).
- [14] C. A. Hummel, D. Mozurkewich, N. M. Elias II, A. Quirrenbach, D. F. Buscher, J. T. Armstrong, K. J. Johnston, R. S. Simon, D. J. Hutter, *Astron. J.* **108**, 326 (1994).
- [15] A. Labeyrie, *Ann. Rev. Astron. Astrophys.*, **16**, 77–102, (1978).
- [16] P. R. Lawson ed., *Principles of Long Baseline Stellar Interferometry*, 1999 Michelson Summer School, JPL Publication 00-09, (2000).
- [17] M. Shao, M. M. Colavita, *Ann. Rev. Astron. Astrophys.*, **30**, 457–498, (1992).
- [18] F. Roddier, *Phys. Rep.*, **170**(2), 97–166, (1998).
- [19] S. G. Lipson, H. Lipson, D. S. Tannhauser, *Optical Physics*, Cambridge University Press, (1995).
- [20] M. Born and E. Wolf, *Principles of Optics*, Pergamon Press, (1964).
- [21] R. S. Longhurst, *Geometrical and Physical Optics*, Longmans, (1957).
- [22] A. Yance, M. P. J. L. Chang, *Computing Research Conference 2002*, March 16, 2002

- [23] K. R. Lang, *Astrophysical Formulae*, Vol II, Springer Verlag, (199).
- [24] *Polarization Effects*. Appendix D from Report of “Phase B” engineering study (supported under NSF Cooperative Agreement 90-08941) for the CHARA array.
<http://www.chara.gsu.edu/CHARA/techreport.html>
- [25] CHARA Technical Report No. 28 2 february 1996.
<http://www.chara.gsu.edu/CHARA/techreport.html>